

OPTIMIZATION OF METALIZATION IN
CRYSTALLINE SILICON SOLAR CELLS

A THESIS SUBMITTED TO
THE GRADUATE SCHOOL OF NATURAL AND APPLIED SCIENCES
OF
MIDDLE EAST TECHNICAL UNIVERSITY

BY

OLGU DEMİRCİOĞLU

IN PARTIAL FULFILLMENT OF THE REQUIREMENTS
FOR
THE DEGREE OF MASTER OF SCIENCE
IN
MICRO AND NANOTECHNOLOGY

AUGUST 2012

Approval of the Thesis:

**OPTIMIZATION OF METALIZATION IN
CRYSTALLINE SILICON SOLAR CELLS**

Submitted by **OLGU DEMİRCİOĞLU** in partial fulfillment of the requirements
for the degree of **Master of Science in Micro and Nanotechnology**
Department, Middle East Technical University by,

Prof. Dr. Canan Özgen
Dean, Graduate School of **Natural and Applied Sciences** _____

Prof. Dr. Mürvet Volkan
Head of Department, **Micro and Nanotechnology** _____

Prof. Dr. Raşit Turan
Supervisor, **Physics Dept., METU** _____

Assist. Prof. Dr. H. Emrah Ünalın
Co-Supervisor, **Metallurgical and Materials Eng. Dept.,
METU** _____

Examining Committee Members:

Prof. Dr. Çiğdem Erçelebi
Physics Dept., METU _____

Prof. Dr. Raşit Turan
Physics Dept., METU _____

Prof. Dr. Mehmet Parlak
Physics Dept., METU _____

Assist. Prof. Dr. H. Emrah Ünalın
Metallurgical and Materials Engineering Dept., METU _____

Dr. Mete Çubukçu
Institute of Solar Energy, Ege University _____

Date: 09.08.2012

I hereby declare that all information in this document has been obtained and presented in accordance with academic rules and ethical conduct. I also declare that, as required by these rules and conduct, I have fully cited and referenced all material and results that are not original to this work.

Name, Last Name: Olgu Demircioğlu

Signature :

ABSTRACT

OPTIMIZATION OF METALIZATION IN CRYSTALLINE SILICON SOLAR CELLS

Demirciođlu, Olgu

M. Sc. Department of Micro and Nanotechnology

Supervisor : Prof. Dr. Rađit Turan

Co-Supervisor : Assist. Prof. Dr. H. Emrah Ünalan

August 2012, 103 pages

Production steps of crystalline silicon solar cells include several physical and chemical processes like etching, doping, annealing, nitride coating, metallization and firing of the metal contacts. Among these processes, the metallization plays a crucial role in the energy conversion performance of the cell. The quality of the metal layers used on the back and the front surface of the cell and the quality of the electrical contact they form with the underlying substrate have a detrimental effect on the amount of the power generated by the cell. All aspects of the metal layer, such as electrical resistivity, contact resistance, thickness, height and width of the finger layers need to be optimized very carefully for a successful solar cell operation.

In this thesis, metallization steps within the crystalline silicon solar cell production were studied in the laboratories of Center for Solar Energy Research and Application (GÜNAM). Screen Printing method, which is the most common metallization technique in the industry, was used for the metal layer formation. With the exception of the initial experiments, 6" wafers, which are the industry standard today, were used throughout this work.

Typically, screen printing method includes 3 different printing steps on both rear and front surfaces with operating parameters such as squeegee pressure, squeegee speed and snap off. In this study, we have concurrently studied multiple parameters that would affect the metal functionality like aspect ratio, uniformity, thickness, resistance and shadow losses. We also studied the back surface field formation by the aluminum diffusion on the back side of the cell.

Subsequent to the printing optimization, drying and firing steps of the metallization were also studied. The improvement in the metallization alone has led to an increase in the efficiency of the cell and a photon conversion efficiency of 15.26 % was obtained. Quality control studies conducted with Ferro GmbH proved the accuracy and the efficiency of the screen printing process carried out at GUNAM. With the improvements in other processes like laser edge isolation, we have reached to an efficiency value of 17 % at GÜNAM Laboratories

Recent advances in PV technologies are based on new cell designs such as back contact solar cells, buried contact solar cells, metallization through solar cells and selective emitter solar cells. All these new technologies employ new metallization schemes that enhance the cell performance. These new cell designs and other new innovative approaches will be the subject of our future studies.

Keywords: Solar Cell, Metallization, Photovoltaic Technology, Screen Printing

ÖZ

KRİSTAL SİLİSYUM TABANLI GÜNEŞ GÖZELERİNİN METALİZASYON OPTİMİZASYONU

Demirciođlu, Olgu

Yüksek Lisans, Mikro ve Nanoteknoloji Bölümü
Tez Yöneticisi : Prof. Dr. Raşit Turan
Ortak Tez Yöneticisi : Yrd. Doç. Dr. H. Emrah Ünal

Ağustos 2011, 103 sayfa

Kristal Silisyum tabanlı güneş gözelerinin üretimi aşındırma, katkılama, tavlama, silisyum nitrat kaplama, metal kontak atma ve yakma gibi birçok fiziksel ve kimyasal işlemlerden oluşur. Bu işlemler arasından metalizasyon, gözenin enerji çevrim performansı açısından büyük önem taşımaktadır. Atılan metallerin kalitesi ve üzerine altlık ile arasında oluşan elektriksel temas yüzeyinin kalitesi göze tarafından üretilen enerji miktarı üzerinde oldukça etkindir. Yüksek performansa sahip bir güneş gözesi yapılabilmesi için tüm bu metal kontakların elektriksel dirençleri, kontak dirençleri, kalınlıkları, atılan elektrotların en ve boyları dikkatli bir şekilde optimize edilmelidir.

Bu tez çalışmasında, Güneş Enerjisi Araştırma ve Uygulama (GÜNAM) laboratuvarlarında kristal silisyum güneş gözelerinin metalizasyon işlemleri optimize edilmiştir. Bu çalışmada metalizasyon yöntemlerinden endüstride en sık kullanılan serigrafi (elek baskı) yöntemi kullanılmıştır. Yapılan ilk deneyler dışındaki tüm optimizasyon çalışmalarında endüstriyel boyut olan 6 inç (156x156 mm) ebatlarındaki silisyum dilimler kullanılmıştır.

Serigrafi yöntemi genel olarak ön ve arka yüzeyde 3 baskı aşamasından oluşur ve her bir aşama rakle baskısı, rakle hızı ve maske yüksekliği gibi

farklı çalışma deęişkenlerini içerir. Bu optimizasyon çalışmaları kapsamında eşzamanlı olarak yükseklik oranı, tekdüzelik, kalınlık, direnç ve gölge kayıpları gibi farklı metalizasyon işlevlerinin başarılı olması için çalışıldı.

Bası optimizasyonuna müteakip olarak kurutma ve yakma işlemleri üzerine çalışmalar yapıldı. Bu çalışmalar sonucunda GUNAM laboratuvarlarında %15,26 verime ulaşıldı. Ferro şirketi ile ortaklaşa yapılan deneyler neticesinde GÜNAM laboratuvarlarında yapılan serigrafi işlemlerinin hassasiyeti ve kalitesi karşılaştırmalı olarak kanıtlandı.

Fotovoltaik Teknolojilerde arkadan kontaklı güneş gözeleri, gömülü kontaklı güneş gözeleri, metal delikli güneş gözeleri ve seçici yayıcı güneş gözeleri geliştirilmiş metalizasyon temelli göze tasarımlarıdır. Bu çalışmanın devamı olarak verim artışı sağlamak üzere bu tip yenilikçi tasarımların deneysel olarak çalışılması gerekmektedir.

Anahtar kelimeler: Güneş Gözesi, Metalizasyon, Fotovoltaik Teknoloji, Serigrafi

To all my family...

ACKNOWLEDGEMENTS

I would like to thank Professor Rařit Turan for his support, the instructive discussions, and allowing me to work independently. Also I would like to thank Assist. Prof. Dr. Emrah Ünalán for his support as my co-advisor in this research. I am thankful to Dr. Mustafa Kulakçı for sharing his experience and mentoring comments.

I want to send special thanks to Fırat Es for the brainstorming and problem solving sessions. I am privileged to be your colleague. Another special thanks goes to Mehmet Karaman, thank you for being such a supportive friend. It is your “ethy!” support that kept me going. I certainly need that support for the rest of my life.

I am also thankful to my wife for her support and understanding through out my research studies. Special thanks to Dr. Sibel Selçuk for helping with the review process.

I would like to also thank Yücel Eke, this thesis certainly benefitted greatly from his creative solutions to the challenges we came across. I am thankful to Hande Çiftıınar for helping when I needed, Makbule Bilgen and Gülsen Baytemir for their contributions during long printing days. I am also thankful to Banu Kosif and Erdem Katı, this research started with our joint efforts.

Finally I would like to thank my family. I truly appreciate your endless support and patience during long hours of work. I am especially grateful to my wife for her endless support and understanding throughout this period.

TABLE OF CONTENTS

ABSTRACT.....	iv
ÖZ.....	vi
ACKNOWLEDGEMENTS	ix
TABLE OF CONTENTS.....	x
LIST OF TABLES.....	xiii
LIST OF FIGURES	xv
1.INTRODUCTION	1
1.1. Increasing Energy Demand of the World	1
1.1.1. Photovoltaic Technology and the Photovoltaic Market.....	3
1.1.2. History and Future of Photovoltaic Technology	7
1.1.3. Photovoltaic Technology Types	10
1.1.3.1. Crystalline Silicon Photovoltaic Technology	10
1.1.3.2. a-Si Thin Film Photovoltaic Technology	10
1.1.3.3. CIS and CIGS Solar Cells	11
1.1.3.4. CdTe Thin film Solar Cells.....	11
1.1.3.5. Dye Sensitized Solar Cells (DSSC).....	11
1.1.3.6. Organic Solar Cells	11
1.1.4. Summary of the thesis	12
2. PROCESS OF METALLIZATION IN THE C-SI SOLAR CELL TECHNOLOGY.....	13
2.1. Basics of Solar Cell operation	13
2.2. Basic Production Steps of Crystalline Silicon Solar Cells	17

2.2.1. Saw Damage Etching	18
2.2.2. Surface Texturing	19
2.2.3. Doping	19
2.2.4. SiN coating	21
2.2.5. Metallization.....	21
2.2.6. Edge Isolation	22
2.3. Metallization of c-Si Solar Cells.....	22
2.3.1. Metallization Methods	23
2.3.1.1. Screen Printing.....	23
2.3.1.2. Electroless Plating.....	26
2.3.2. Front Metallization.....	26
2.3.2.1. Mathematical Description of the Metallization Pattern.....	29
2.3.2.2. Experimental Approach to Front Surface Metallization.....	31
2.3.3. Back Surface Metallization.....	34
3. EXPERIMENTAL PROCEDURES	37
3.1. Metallization System (Screen Printing)	37
3.1.1. Screen printer	37
3.1.2. Metallization Masks.....	39
3.1.3. Metallization Pastes	41
3.1.4. Drying Furnace	42
3.1.5. Firing Furnace.....	42
3.1.6. Solar Simulator	44
3.2. Contact Resistance Measurements	45
4.1 OPTIMIZATION OF FRONT&BACK SURFACE METALLIZATION OF c-Si SOLAR CELLS BY SCREEN PRINTING.....	48
4.1. Introduction	48

4.2. Contact Resistance	48
4.2.1. Dependence of Contact Resistance on Drying Process	49
4.2.2. Dependence of Contact Resistance on Firing Process	50
4.3. Front Surface Metallization	52
4.3.1. Squeegee Speed	53
4.3.2. Squeegee Pressure	56
4.3.3. Snap Off.....	59
4.3.4. System Stability Test	61
4.3.5. Finger Homogeneity Test.....	62
4.4. Back Surface Metallization.....	64
4.5. Firing Optimization	68
4.5.1. Firing Optimization Experiments	69
A) Experiment 1	70
B) Experiment 2	76
C) Experiment 3	82
D) Experiment 4	84
4.5.2. Back Surface Field optimization.....	88
4.6. Cross Experiments in Ferro GmbH.....	91
4.7. Fabrication of a High Efficiency Solar Cell at GÜNAM Laboratories	93
5. CONCLUSION	97
REFERENCES	100

LIST OF TABLES

TABLES

Table 2.1: Resistive losses according to M. Green [22]	31
Table 3.1 Properties of masks which are used in this study.	40
Table 4.1 Finger height and width data taken from points A,B,C and D.....	53
Table 4.2 Average Finger dimensions with respect to Squeegee Speed.....	54
Table 4.3 Average Finger dimensions with respect to Squeegee Pressure. 57	
Table 4.4 Height Deviation depending on printing parameters.	63
Table 4.5 Sample Firing Furnace parameters for experiment 1.....	70
Table 4.6 Firing parameters of Set 1, Set 2 and Set 3 of experiment 1.	70
Table 4.7 Results of experiment 1, set 1.....	71
Table 4.8 Results of experiment 1, set 2.....	73
Table 4.9 Results of experiment 1, set 3.....	76
Table 4.10 Firing parameters of the samples which are used in experiment 2	77
Table 4.11 Results of experiment 2, Set 1	78
Table 4. 12 Results of experiment 2, Set 2	80
Table 4. 13 Results of experiment 2, set 3.....	81
Table 4.14 Experimental conditions giving bumps and bows on the back Al metal layer.	83

Table 4.15 Firing temperatures and corresponding cell parameters obtained from the I-V curves of the samples fabricated using paste B.	84
Table 4.16 Applied recipes and obtained sheet resistances.	89
Table 4. 17 Sets of cross experiment with Ferro GmbH and GÜNAM	92
Table 4.18 Average efficiency results of cross experiments	92

LIST OF FIGURES

FIGURES

Figure1.1 Increasing energy demand of the world [1].....	2
Figure1.2 Direct relations between the decrease on both raw silicon material and PV prices [2].....	4
Figure1.3 Projection of PV electricity prices with respect to existing grid parity [3].....	5
Figure1.4 Installed PV capacities between 2000-2011 through the world. Orange: Europe and Yellow: Rest of the world [5]	6
Figure1.5 PV installation in 2011 in top countries [5].	7
Figure1.6 Solar Cell Shipments in 2010.....	9
Figure 2.1 Ideal I-V curve of a diode under dark and illuminated conditions [14].....	14
Figure 2. 2 An example of a solar cell I-V curve [16].....	15
Figure 2. 3 Effect of R_S and R_{SH} on solar cell I-V curve [17]	17
Figure 2.4 Process chain of c-Si.	18
Figure 2.5 p-n junction formation and photo-generated carrier flows.	20
Figure 2.6 Band diagram of a p-n junction.	20
Figure 2.7 Schematics of screen printing method. General view of the screen (a), Cross section view of screen printing system before (b) and after (c). ..	24

Figure 2.8 Cross sectional view of a screen printed line. (a) Realistic cross section. (b) Ideal cross section to reduce both series resistance and shadow effect.	25
Figure 2.9 Different schematic versions of H-bar front contact designs. (a) Standard H-bar design with 2 busbars, (b) Standard H-Bar design with 3 busbars, (c) H-bar design with busbars at edges.....	27
Figure 2.10 Metal Wrap Through Design, (a) Photograph of a MWT Solar Cell manufactured by Solland Solar [20]. (b) Schematic cross section view of a MWT Solar cell.....	28
Figure 2.11 Schematics for (a) a standard screen printed solar cell cross-section and (b) buried contact solar cells cross-section.....	29
Figure 2.12 Dimensions of fingers and busbars on solar cell.....	30
Figure 2. 13 Finger height profiles of GÜNAM cells measured in FERRO GmbH Labs.....	32
Figure 2.14 Electroluminescence image of a standard GUNAM Cell with 16% efficiency.....	33
Figure 2. 15 Back surface metallization of a standard 6 inches c-Si solar cell.	34
Figure 3.1 a) Photograph of screen printer used in this work, b) snapshot of the system software	37
Figure 3.2 Schematic showing squeegee pressure, squeegee speed.....	39
and snap off	39
Figure 3.3 a) Back busbar mask, b) back aluminum mask, c) front Ag Mask. Black areas are mesh openings.....	40
Figure 3.4 Sample image of a screen printing mesh [28].....	41

Figure 3.5 Recommended sample firing temperature profile [29]	43
Figure 3.6 a) Photograph of firing furnace used in this study and b) a snapshot of the control software.	44
Figure 3.7 Photograph of solar simulator and snapshot of the simulator software	45
Figure 3.8 a) Contact geometry and b) Sample TLM Graph [32]	46
Figure 4.1 Contact resistance of Al paste on Si wafer as a function drying temperature and time.....	49
Figure 4.2 Contact resistance of Ag paste on Si wafer as a function of drying temperature and time.....	50
Figure 4.3 Contact resistance of Al paste on Si wafer as a function of firing temperature and speed.....	51
Figure 4.4 Contact Resistance of Ag paste on Si wafer as a function of firing temperature and time.....	52
Figure 4.5 Squeegee speed dependence of average finger width.....	54
Figure 4.6 Squeegee speed dependence of average finger height.....	55
Figure 4.7 Squeegee Speed dependence of average aspect ratio.	55
Figure 4.8 Plot of average finger widths vs. squeegee pressure.....	57
Figure 4.9 Plot of average finger heights vs. squeegee pressure.	58
Figure 4.10 Plot of aspect ratio vs. squeegee pressure.	58
Figure 4.11 Plot of average finger widths vs. snap off.	59
Figure 4.12 Plots of average finger heights vs. snap off.	60
Figure 4.13 Plots of aspect ratio vs. snap off.	60

Figure 4.14 Finger height and widths of the samples, which printed with same parameters.....	61
Figure 4.15 Finger homogeneity test method by Dek-Tak Profilometer.	62
Figure 4.16 Surface profile of a finger.....	64
Figure 4.17 Photograph of conventional & modified of back Al masks.	65
Figure 4.18 Non-homogeneity problem of Al contact.....	66
Figure 4.19 Squeegee pressure dependence of Al metal paste mass.....	67
Figure 4.20 Squeegee speed dependence of Al metal paste mass.	67
Figure 4.21 Snap off dependence of Al metal paste mass.....	68
Figure 4.22 I-V curves of sample 3,4,5 with hot zone speed 50 mm/s, 75 mm/s and 100 mm/s while entrance speed is 25 mm/s. Peak temperature was 870°C (Cell area was 92.5 cm ²).....	71
Figure 4.23 I-V curves of sample 6,7,8,9 with hot zone speed 25mm/s, 50 mm/s, 75 mm/s and 100 mm/s while entrance speed is 100 mm/s. Peak temperature is 870°C. Cell area is 92.5 cm ²	73
Figure 4.24 I-V curves of sample 10,11,12 and 13 with hot zone speed 25mm/s, 50 mm/s, 75 mm/s and 100 mm/s while entrance speed is 100 mm/s. Peak temperature was 910°C. Cell Area was 92.5 cm ²	75
Figure 4.25 I-V curves of sample 2, 3, 4 with conveyor speed 70 mm/s, 80 mm/s and 90 mm/s, while peak temperature was 870°C. Cell area was 92.5 cm ²	78
Figure 4.26 I-V curves of sample 5, 4, 6 respectively with peak temperatures 860°C, 870°C and 880°C, while conveyor speed was 90mm/s. Cell area was 92.5 cm ²	79
Figure 4.27 Bump problems on back Al paste.	80

Figure 4.28 I-V curves of sample 8,7,2 respectively with peak temperatures 850°C, 860°C and 870°C, while conveyor speed was 70mm/s. Cell area was 92.5 cm ²	81
Figure 4.29 Peak temperature dependency of open circuit voltage and short circuit current.	85
Figure 4.30 Peak temperature dependence of fill factor and efficiency.....	85
Figure 4.31 EDX results of pastes a) Al paste before firing b) Al paste after firing c) Ag paste before firing d) Ag paste after firing.....	87
Figure 4.32 Firing dependence of back surface sheet resistance.	89
Figure 4.33 Conveyor speed dependence of back surface field depth.	90
Figure 4.34 Firing temperature dependence of back surface field depth.	90
Figure 4.35 Finger homogeneity characterization of a sample from Set 1. ...	93
Figure 4.36 Front and back view of 17 % efficient solar cell fabricated in GÜNAM Laboratories.....	94
Figure 4.37 I-V Curve of highly efficient c-Si solar cell.....	95
Figure 4. 38 Progress in the efficiency values of c-Si solar cells fabricated at GÜNAM Laboratories.....	96

CHAPTER 1

INTRODUCTION

1.1. Increasing Energy Demand of the World

The world's increasing energy demands causes several economic, environmental and political problems. Natural gas, petroleum and coal are the major energy sources that are readily available today. Figure 1.1 summarizes the increasing consumption of energy sources up to date along with the future projections. As a result of increasing demand, unit price of electrical energy are also increasing in liberal economy. Usages of carbon based energy sources also promote global warming. CO₂ emission rate into the nature is more than natural CO₂ to O₂ conversion and this situation causes greenhouse gas depletion and an increase in the average temperature of the atmosphere each year. While these economic and environmental problems are growing, social and political problems arise in the energy dependent countries.

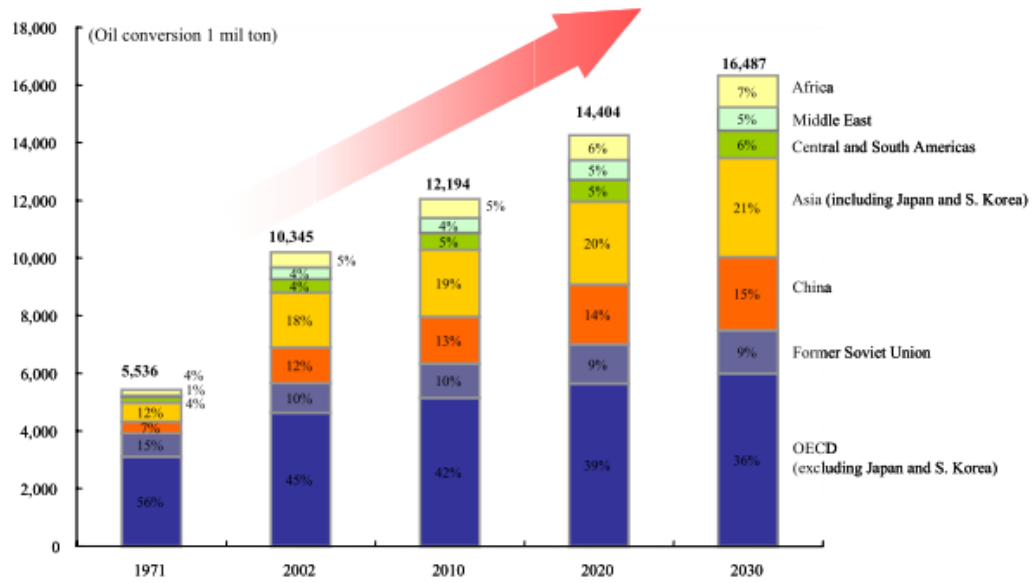


Figure1.1 Increasing energy demand of the world [1]

Not only as an alternative but also as our responsibility for the next generations, new ways of energy production should be provided. Indeed there are several energy sources such as solar energy, wind energy, wave energy, geothermal energy, etc. However, the critical point is the convertibility of these energies to a common energy type, namely electrical energy. In addition to convertibility by technology, conversion cost should be also competitive with existing electrical energy sources.

Although all other alternative energy sources are available in different geological parts of the world, solar energy attracts more attention because of its abundance, availability and cleanness. With decreasing costs, increasing efficiency and reliability of technology over the few years, it has become even more promising for the future of our society.

1.1.1. Photovoltaic Technology and the Photovoltaic Market

Photovoltaic (PV) Technology is a semiconductor technology mostly based on silicon (Si) material. The most important characteristic of the PV technology is the conversion of solar energy directly to the electrical energy without any intermediate phase. Some other advantages of Photovoltaic Technology are:

- No moving parts: PV panels are static elements and don't have any moving parts such as gears or pistons found in turbines or wind energy generators. This difference keeps PV systems' operating cost lower than others. For the same reasons, systematic failures are less likely than mechanical systems.
- Environment friendly technology: during the operation of PV panels, CO₂/CO emission does not occur. In addition to zero carbon emission, PV panels based on Si do not contain any poisonous materials in it. Si is derived from pure sand.
- Noise free systems: PV systems do not have any noise. So it makes PV panels usable on roof tops or city centers without any noise pollution.
- Large/Small scale applications: there is not much economical threshold to build up a PV system. They can be installed as a roof top (5-6 KW scale) to supply the demand for a household or can be installed as large scale power stations (10-200 MW scale) to supply the demand for the city electricity.

Photovoltaic technology is known as an "expensive investment". However, recent reports show that the raw material prices have decreased dramatically in recent years. Figure 1.2 shows the decrease in the cost of the raw materials and PV Systems.

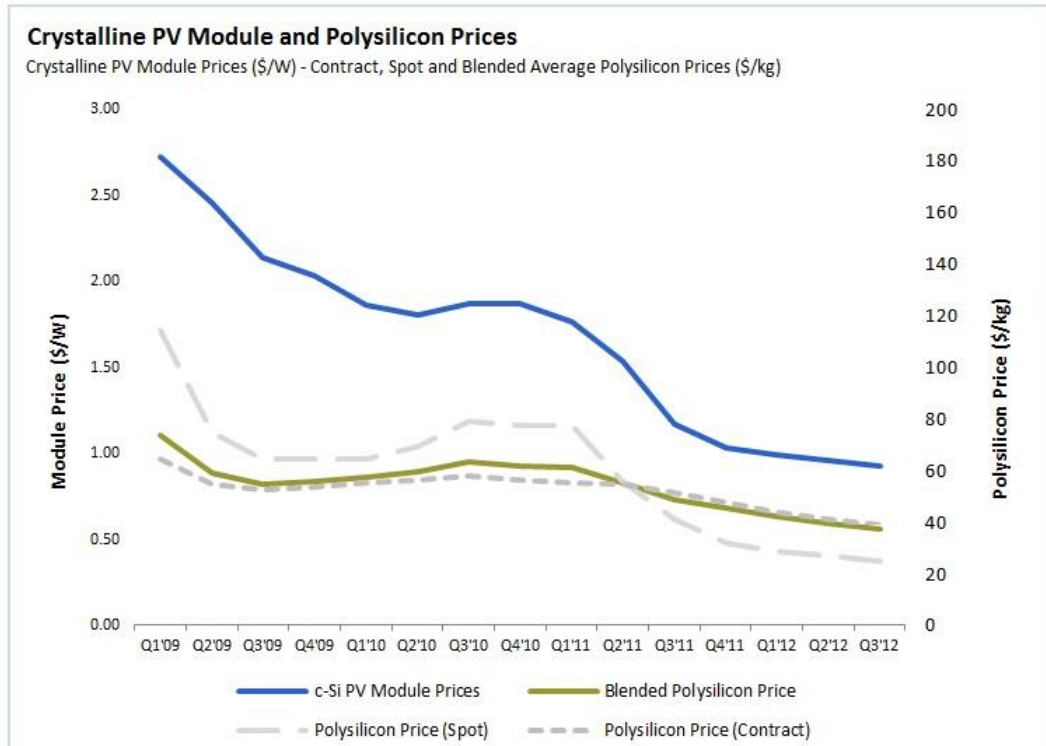


Figure 1.2 Direct relations between the decrease on both raw silicon material and PV prices [2].

Not only solar grade Si prices but also silver metal paste prices, and production equipment prices are also decreasing. As mentioned before, compatibility with other electricity production cost rates is the most important point. Figure 1.3 presents the past evolution and future estimation of the PV electricity price in comparison with the conventional energy sources as reported by Prof. Sach.

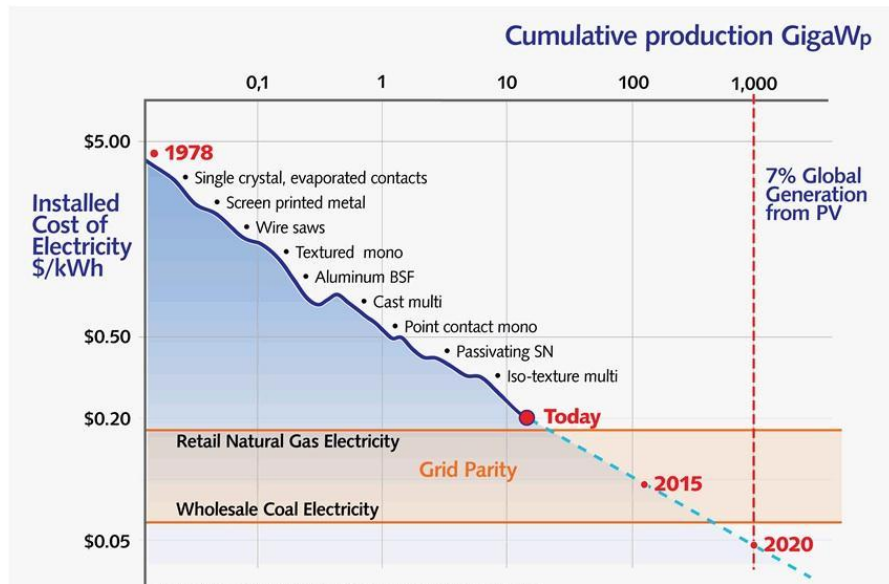


Figure1.3 Projection of PV electricity prices with respect to existing grid parity [3].

We see that photovoltaic costs decreased with the developments in the production methods, such as application of screen printing for metallization and some optimized chemical processes during the past 30 years. Today PV cost per kWh is about \$0.22 while retail Natural Gas electricity cost is \$0.18 and wholesale Coal electricity is \$0.07 in US. In Turkey, PV cost per kWhs is about \$0.07-0.08 while Natural Gas electricity cost is \$0.069 and coal electricity cost is \$0.01. According to the projection given in Figure 1.3, PV electricity will be cheaper than natural gas electricity in 3-4 years and cheaper than Coal Electricity by 2020. This projection overlaps with the European Commission's 2020 projection, which includes the production of 20% energy demand of Europe from renewable energy sources [4].

Increase on demand can be also seen on the amount of installed PV capacity given in Figure 1.4.

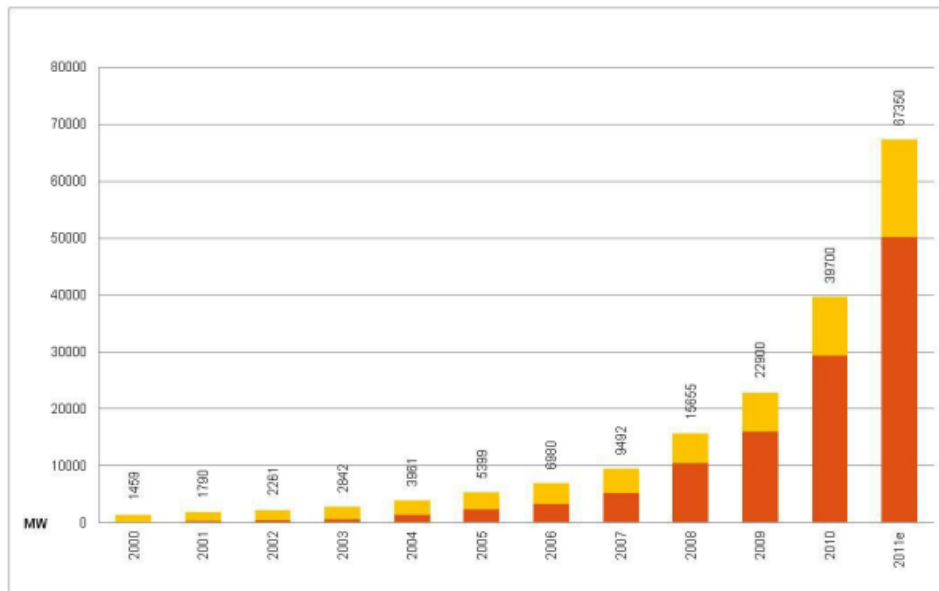


Figure1.4 Installed PV capacities between 2000-2011 through the world.
Orange: Europe and Yellow: Rest of the world [5]

The race on PV installation has continued in 2011 with an unpredicted record. In 2011 totally 27.65 GW PV system installed all over the world. As shown in Figure 1.4, 33% of this installation was in Italy followed by Germany with an installation rate of 27%.

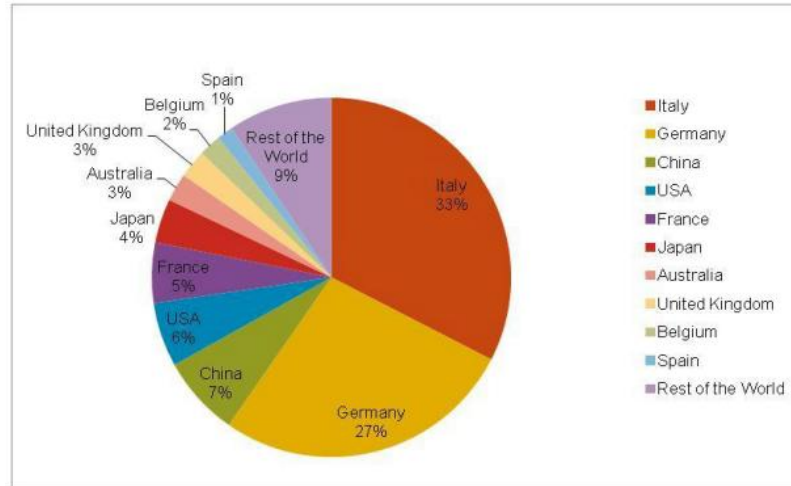


Figure1.5 PV installation in 2011 in top countries [5].

2011 European Photovoltaic Industry Association (EPIA) Market Report shows that Italy is number one on the PV installation in 2011, while Germany is still pioneering in cumulative. It is interesting that Slovakia and Ukraine have also started to install PV systems although their solar irradiation is much less than Turkey. Despite its high solar radiation, Turkey is still not among the major PV installing countries.

1.1.2. History and Future of Photovoltaic Technology

Light-Matter interaction has always been an interesting subject in physics. It was first observed by Edmund Becquerel in 1839 [6]. However, this phenomenon was first described by Einstein in 1923 as Photoelectric Effect [7]. Although first single crystalline structure was produced from Si in 1918, first p-n junction was fabricated on germanium crystal. First prototype Si solar cell was produced in Bell Laboratories in 1955. In the following years Hofmann Industry started to produce first solar cells to use them in space industry. In the next 20 years, space industry was the only target for photovoltaic industry [6]. Only after the start of the new century, PV cells were seen as an alternative to the conventional fossil fuels for large scale

energy production. Thanks to the various incentive mechanisms introduced by developed countries and intensive research and development activities that have led to dramatic cost reduction.

In this journey many milestones were reached and new ones were set up. For instance, reducing the thickness of wafer enhanced the V_{oc} (Open Circuit Voltage) of cells. By this way, first crystalline thin film Si solar cell and amorphous Si solar cells were fabricated. First commercial amorphous Si solar cells were in the market by 1981 [8].

Today, with the help of material science, a lot of photovoltaic materials and devices have been designed and produced. Some of them have found shares in the commercial market. The market shares of the present PV technologies are shown in Figure 1.6. As seen from this figure, solar cells based on, crystalline or amorphous Si, heterojunction structures, CIS(Copper Indium Selenium), CIGS(Copper Indium Gallium Selenium) are available in the commercial market. In addition to those shown in Figure 1.6, new materials based on dye sensitized composites and polymers are being heavily studied to fabricate so-called Dye Synthesized Solar Cells (DSSC) and organic solar cells, respectively. Some of these new designs have already been commercialized in recent years [8].

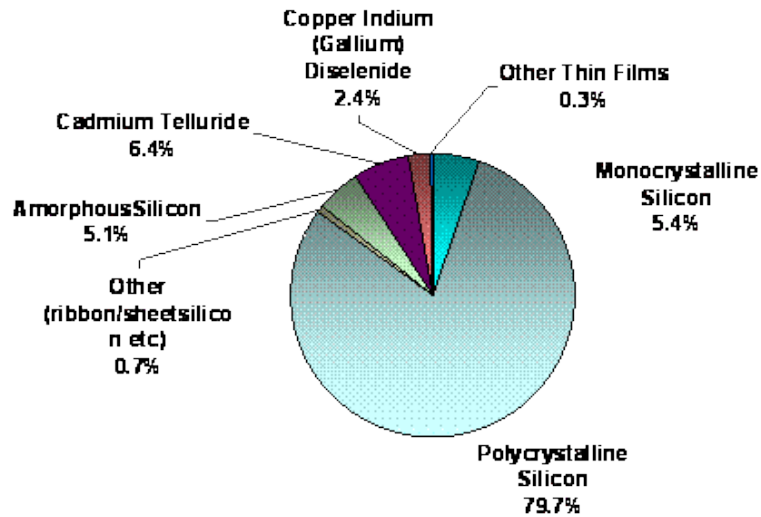


Figure 1.6 Solar Cell Shipments in 2010

The crystalline Si (c-Si) solar cells overwhelmingly dominate the PV market today due to proven reliability, stability in harsh environment for many years and high efficiency. Intensive research efforts have been spent on the improvement of c-Si solar cells. In spite of these improvements created by scientific and industrial research activities, there is still a room for further improvements. Present world record for Si solar cells is at around 25%, which is well below the theoretical limit (known as Shockley-Queisser limit) of 35% for c-Si. This difference can be reduced with research focused on reducing loss of carriers generated by the solar radiation. One of the issues is to eliminate the losses due to the metal contacts to collect the charge carriers. Metal contacts cover the front side and the back side of the cell and provide the connection between the solar cell and the outside world. They play a critical role in transferring the generated carriers to the outside circuitry. Any problem caused by the metal contacts such as excessive series resistance, and shadowing effects on the front side, may lead to a reduction of the cell efficiency.

1.1.3. Photovoltaic Technology Types

Over the past 30 years, different photovoltaic technologies have been developed. While c-Si solar cells are still dominant in the market, thin film technologies, organic and dye sensitized solar cell are also promising. Some of them have been commercialized and some of them are still under research in laboratories and waiting for further developments.

1.1.3.1. Crystalline Silicon Photovoltaic Technology

c-Si cells dominate most of the world market by more than %85 [9]. Reliability of the technology, low production investment and slowly increasing efficiencies make this technology popular. c-Si PV cells are divided to in sub categories based on the crystallinity of the wafer: mono-crystal and multi crystal. Mono-crystalline wafer means that the entire wafer is in a single crystal form edge to edge. Multi-crystalline wafer consist of different crystalline domains with different crystal orientation. Although the boundary regions between crystalline domains decrease the cell efficiency, low production cost of multi crystalline wafers makes this material competitive to the mono crystalline wafers.

1.1.3.2. a-Si Thin Film Photovoltaic Technology

Instead of using bulk Si crystal, thin film Si is also a good alternative to convert solar energy to electrical energy. Si crystal is the major cost item in solar cell production. For this reason reducing the amount of Si is necessary to reduce the solar cell costs. The reduced thickness of the Si brings some disadvantages such as low light absorption. For this reason p-i-n structure is developed including intrinsic Si layer between classical p-n junction. By optimizing the crystallinity of the deposited thin film Si layers, it is possible to adjust band gap of the material between 1.7-2.1 eV [10]

1.1.3.3. CIS and CIGS Solar Cells

With the development of thin film technology, different thin film photovoltaic devices have been developed. Copper Indium Selenide (CIS) and Copper Indium Gallium Selenide (CIGS) solar cells are also known as chalcopyrite solar cells because of their chemical structure. Today the most efficient thin film solar cells in the market are CIGS solar cells [11]. Direct band gap of the CIGS make them special with respect to Si solar cells. In addition, since CIGS solar cells can be deposited onto flexible substrates, new application areas are possible for this PV type.

1.1.3.4. CdTe Thin film Solar Cells

Cadmium Telluride (CdTe) material is another popular material which is used in PV industry. Low cost and high solar absorption with a band gap 1.5 eV makes it a popular commercial product in the market. CdTe solar cells consist of CdTe substrate and Cadmium Sulfide (CdS) emitter layer to create p-n junction.

1.1.3.5. Dye Sensitized Solar Cells (DSSC)

Dye sensitized solar cells are excitonic solar cells with very low production costs. Although their efficiencies and lifetimes are very low, ease of production makes this technology commercially attractive. It is possible to make those cells semi-transparent and colorful. So, DSSC technology has an esthetic advantage for variable applications.

1.1.3.6. Organic Solar Cells

As it is in all R&D branches, polymers are convenient to produce photovoltaic devices. Although they have a major problem like light induced degradation, organic solar cells provide a promising technology for the near future of photovoltaic industry. There are different types of organic device designs with different polymer materials. Main problem about organic solar cells are their low quantum efficiency and instability problems of the materials [12].

1.1.4. Summary of the thesis

This work focuses on the various aspects of the metallization processes used in the production of c-Si solar cells. In Chapter 2, we summarize the basics of solar cell operation, basics production steps of c-Si solar cells and basic knowledge about the metal contacts to c-Si solar cells. In Chapter 3, experimental setup, equipment and their technical properties are introduced. Optimization studies on screen printing processes and firing processes are given in Chapter 4 in details. Results of optimization studies and cross experiment which are performed in Germany and GÜNAM are also discussed in Chapter 4. In Chapter 5, conclusions based on the results obtained from the experiments and future works are presented.

CHAPTER 2

PROCESS OF METALLIZATION IN THE C-SI SOLAR CELL TECHNOLOGY

2.1. Basics of Solar Cell operation

A solar cell device is a large area electronic diode formed by combining p-type and n-type Si materials [13]. The formed p-n junction creates a built-in electric field which plays a key role in the diode operation. The current-voltage (I-V) characteristics of a p-n junction diode under illumination is given by

$$I = I_0 \left(e^{qV/nkT} - 1 \right) - I_{ph} \quad \text{Eqn. (2.1)}$$

where I_{ph} is the photocurrent generated by illumination. The I-V curves corresponding to dark and illuminated conditions are given in Figure 2.1.

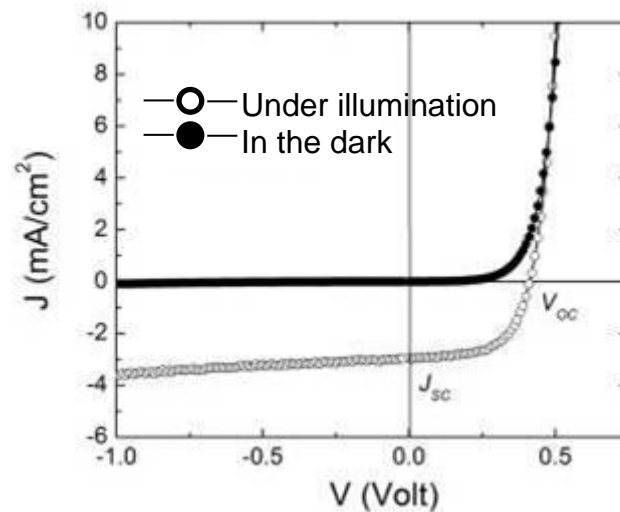


Figure 2.1 Ideal I-V curve of a diode under dark and illuminated conditions [14].

The I-V curve shifts under illumination because of the photogenerated carriers inside the semiconductor material. These photogenerated carriers are the basis for the power generation in a solar cell.

In order to characterize a solar cell, the 4th quadrant of I-V curve is studied. When this quadrant is reversed and sketched separately, the classical solar cell I-V curve is obtained as shown in Figure 2.2.

Basic electrical parameters of a solar cell are open circuit voltage (V_{oc}), short circuit current (I_{sc}), maximum power point, maximum power voltage (V_{mp}) and current (I_{mp}), fill factor, efficiency, series resistance and shunt resistance. All of these parameters can be seen or derived from the I-V curve of the solar cell.

Basically these properties are;

- *Open circuit Voltage (V_{oc}):* V_{oc} is the voltage obtained from the cell when there is no current flow over the cell and load [15]. V_{oc} of a

standard c-Si solar is between 0.61-0.62 volts. However, this voltage decays with increasing current as seen Figure 2.2.

- *Short Circuit Current (I_{SC}):* This is the current obtained when the solar cell is short circuited [15]. The voltage difference between the terminals of the cell is zero under this condition. Short circuit current can be found from the intersection of the curve with vertical axis.
- *Maximum power point:* Electrical power of the cell is the multiplication of output voltage and output current. The maximum power point is the point at which $I \times V$ has the maximum value.

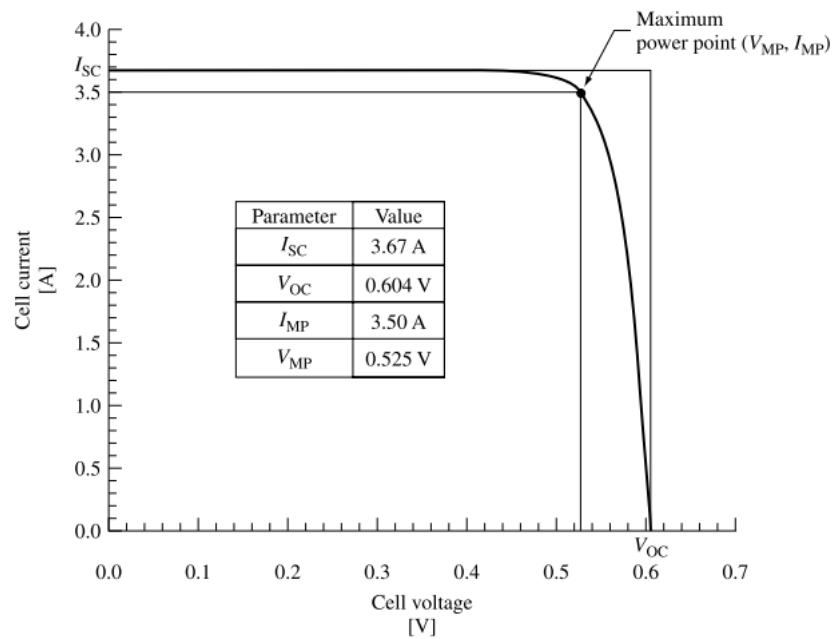


Figure 2. 2 An example of a solar cell I-V curve [16].

- *Maximum power point voltage (V_{MP}):* It is the voltage when maximum power is obtained from the cell. This voltage is important when the cell is connected to a load.

- *Maximum power point current (I_{MP}):* It is the current when maximum power obtained from the cell.
- *Fill Factor(FF):* Fill factor is the ratio of peak power to ($V_{OC} \times I_{SC}$) [16]. Fill factor is a measure of the quality of the solar cell. Fill factor approaches 100% when the solar cells approaches ideal conditions.

$$FF = \frac{\text{Max. Output Power}}{V_{OC} \times I_{SC}} \times 100 = \frac{V_{MP} \times I_{MP}}{V_{OC} \times I_{SC}} \times 100 \quad \text{Eqn. (2.2)}$$

- *Efficiency:* There are different efficiency definitions; but, most basic definition is the ratio of the electrical output power to the optical illumination power. Efficiency of a solar cell is usually given under specific radiation conditions. The most widely used standard for the radiation is so-called AM1.5 condition which correspond to a total power of 1000 W/m^2 . The spectral distribution of the light source used for this purpose should have the same properties as the solar radiation. Solar simulators, which are used in this study are calibrated to AM1.5 conditions.

$$Eff = \frac{\text{Max. Output Power}}{\text{Illuminated Optical Power}} \quad \text{Eqn. (2.3)}$$

- *Series Resistance (R_S):* Seri consist of three different resistance mechanisms: contact resistance in metal-semiconductor interface, ohmic resistance in metal contacts and ohmic resistance in semiconductor material [16]. It is defined as

$$R_{total} = 2xR_c + R_m + R_{semi} \quad \text{Eqn. (2.4)}$$

where R_c is contact resistance, R_m is the resistance of metal contacts and R_{semi} is the resistance of the semiconductor material.

- Series resistance of a cell can be calculated from the vertical part of the I-V curve as shown in Figure 2.3.
- Shunt resistance (R_{SH}): Shunt resistance is the resistance of the cell against reversed leak currents. Reason of the leak currents are edges of the cells, interruptions in p-n junction or overdiffusion of front metal contacts through the junction. Shunt resistance of a solar cell can be calculated from the relation:

$$R_{SH} = \frac{dI}{dV}, \text{ at } V = 0 \quad \text{Eqn. (2.5)}$$

- It can be calculated from the horizontal part of the I-V curve as shown in Figure 2.3.

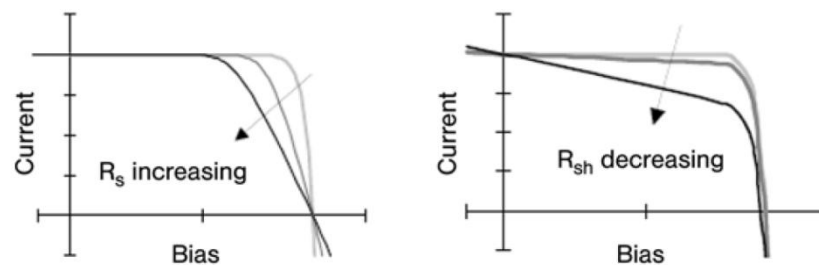


Figure 2. 3 Effect of R_S and R_{SH} on solar cell I-V curve [17]

2.2. Basic Production Steps of Crystalline Silicon Solar Cells

In this section a summary of basic process steps in c-Si solar cells is given for the sake of completeness. A more detailed description of the metallization is provided as a background of the topics studied in this thesis work.

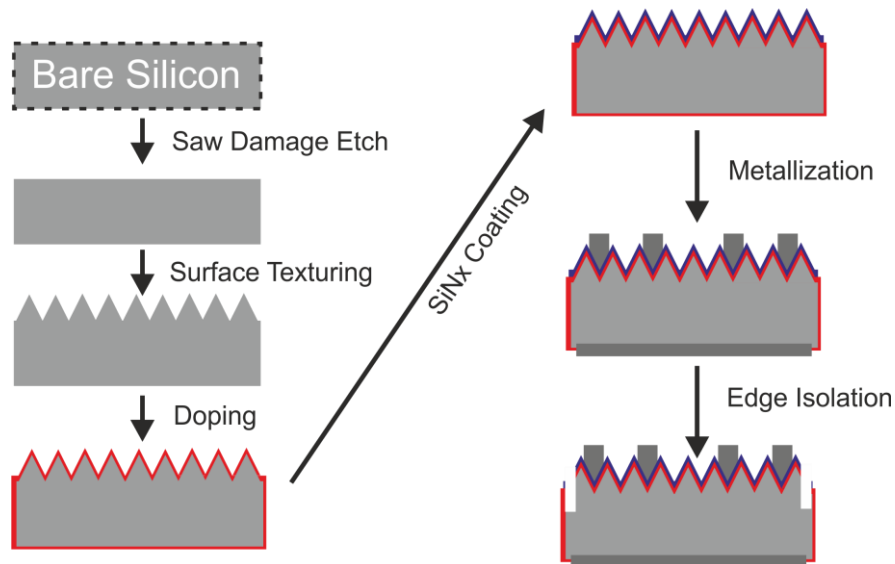


Figure 2.4 Process chain of c-Si.

The process flow chart for the c-Si solar cell fabrication is shown in Figure 2.4. All of these processes can be carried out at the GÜNAM facilities. Most of them have been optimized to obtain high efficiency solar cells.

2.2.1. Saw Damage Etching

At the beginning of the production, c-Si is grown as ingots by either so-called Czochralski or float zone technique. To obtain wafers, these ingots should be cut into thin slices. Generally wire cutting method is used to obtain wafers. However, this cutting process damages the wafers surface in micro level. Sodium hydroxide (NaOH) or potassium hydroxide (KOH) based chemical solutions are commonly used these damages after the wire cutting process [18].

2.2.2. Surface Texturing

Light trapping is needed to enhance the light absorption in the bulk Si. The most common light trapping method is the surface texturing by creating pyramids on the surface. Reflected light from the surface of a pyramid, travels to another pyramid instead of reflecting directly into the air as it is on a flat surface. Second reflection of the light increases the amount of absorbed solar energy.

Creation of surface pyramids are done by wet chemical process: anisotropic KOH etching. KOH etches (100) and (110) surfaces of the Si crystal with and higher rate with respect to (111) surface. By the anisotropy of this etching, it is so easy to create pyramids with (111) surfaces. Density of these pyramids should be optimized with KOH solution, etching time and etching temperature.

2.2.3. Doping

Doping is the main step of solar cell production. Si is 4A group element. Doping Si with boron (3A Group) makes it p-type, while doping with phosphorous (5A element) makes it n-type. By the junction formation with p-type and n-type regions in Si, an electrical field forms. This electrical field separates the generated electron-hole pairs from each other and creates the generated photo carriers. A schematic representation of p-n junction formation and the energy band diagram are shown in Figure 2.5 and Figure 2.6, respectively. The flow of photo-generated carriers is also indicated in Figure 2.5.

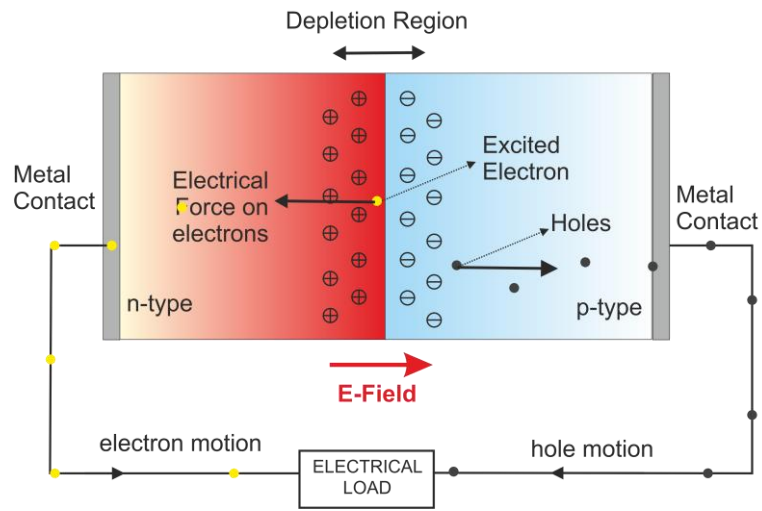


Figure 2.5 p-n junction formation and photo-generated carrier flows.

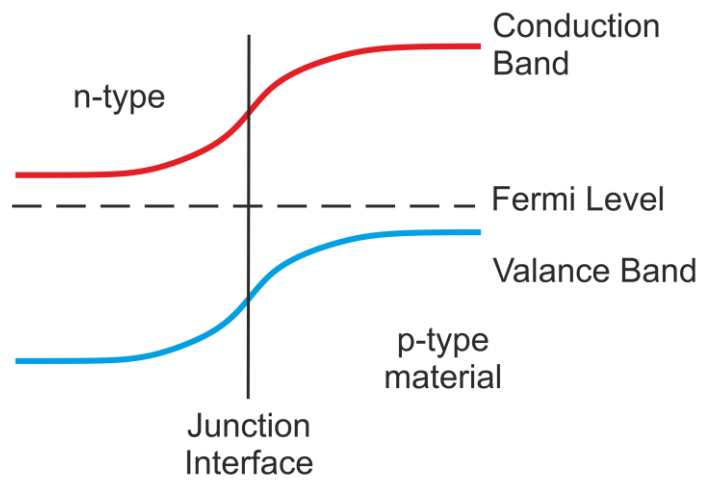


Figure 2.6 Band diagram of a p-n junction.

In c-Si solar cell industry, generally p-type wafers are used initially and p-n junctions are created by the phosphor diffusion in thermal PVD systems. Rarely solar cells based on n-type solar cells are produced.

2.2.4. SiN coating

In this step, the front surface of the doped Si wafer is covered by SiN_x layer (x can be varied depending on the required refractive index). There are 2 main functions of SiN_x layer on the front surface. The first one is to reduce the reflection from the surface, providing further light trapping. Since refractive index of the SiN_x is between refractive indexes of Si (3.4) and air (1), this layer reduces the reflection of sunlight. For the optimum absorption of solar irradiance, reflection coefficient of the SiN_x should be in the range of 1.8-1.9 [19]. Since this coating is not successful to trap the light with blue wavelengths, we see the solar cells in blue color. Second function of the SiN_x layer is front surface passivation. Dangling bonds on the surface generate energy states that cause recombination of excited charge carriers. Recombination reduces the electrical current obtained from the absorption of the sunlight. This loss can be reduced by filling these dangling bonds by the atoms of a passivation layer. SiN_x acts as a good passivation layer for n-type front surfaces.

2.2.5. Metallization

Metallization creates electrodes on p-type and n-type layers of the cell. Different metallization methods and materials are applicable for the c-Si solar cell production. However, most common metallization method in solar cell industry is the screen printing method. Different metals and patterns can be used to create front and rear metal contacts. Firing step should be applied after all printings to induce diffusion of metals into the Si and removing

solvents inside the paste and solidification. Details of the equipment and metallization processes will be covered in Chapter 3.

2.2.6. Edge Isolation

Edge isolation is a necessary step to prevent shunt currents throughout the edge of the Si wafer. Since doping process applied on the front side, back side and edges of the wafer, electrons generated from the emitter layer can flow to back electrode through n-type doped wafer edges. However, the main purpose of the cell is directing the electron flow to back electrode through the circuit. To block shunt currents, front side and rear side of the cell should be isolated. There are several ways to make this isolation. Laser scribing, chemical edge etching and plasma edge etching are common methods for edge isolation.

2.3. Metallization of c-Si Solar Cells

Metallization provides electrical contacts between the solar cells and external load. The most common metallization method is screen printing, which is a suitable method for industrial scale mass production. Rear side of the cell is fully coated by aluminum (Al). With the diffusion of Al (which is a p-type dopant for Si) from the printed Al layer, n-type doped region is converted to p-type again. By this way, p-n junction remains only on the front side. Also diffused Al on the back side of wafer creates Back Surface Field (BSF) to reduce recombination rate on the back side. In addition to the Al coverage, silver/Al bars are printed to enable soldering for external connections.

Front side metallization is a little bit more complicated. A silver (Ag) paste is used instead of Al to keep front side n-type. Full coverage of the surface is not possible to allow light entrance into the cell body. For the front surface metallization, different metal patterns have been used. The most common

pattern, H-bar pattern, consists of fingers and busbars (see Figure 2.9). All dimensions of fingers and busbars should be optimized to minimize series resistance, contact resistance and shadow effect.

Firing step should be applied after all printings for the diffusion of metals into the Si and removing solvents inside the paste and solidification. Firing temperature profile is very sensitive and hard to obtain with convenient furnaces. So, generally belt type furnaces are used for firing.

2.3.1. Metallization Methods

2.3.1.1. Screen Printing

Screen printing is one of the oldest printing methods. Several industries such as textile and glass manufacturing also use screen printing method. Solar cell industry requires more complex and accurate printing than other industries.

Screen printing method consists of a screen with a pattern formed by regions transparent to the paste applied to it. To print a pattern on a substrate, a squeegee is used to force paste through the screen onto the substrate. Details of the system basics can be seen Figure 2.7.

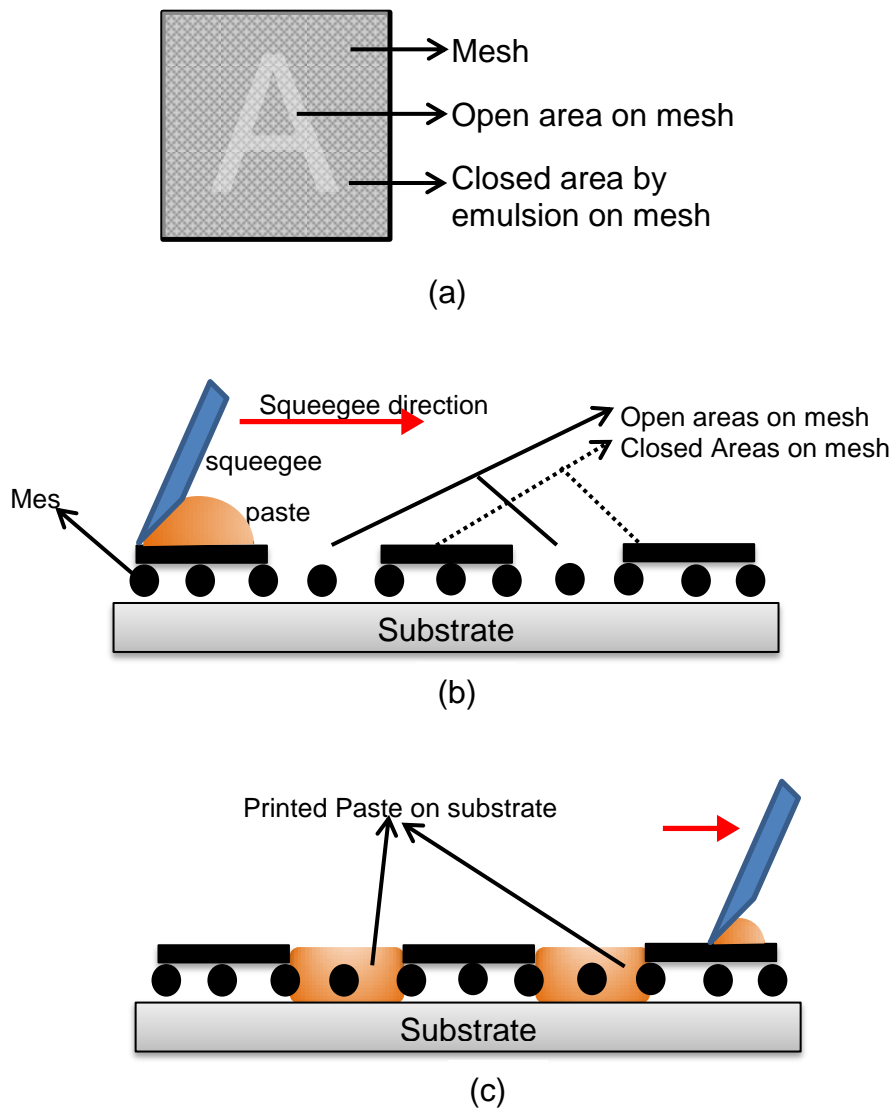


Figure 2.7 Schematics of screen printing method. General view of the screen (a), Cross section view of screen printing system before (b) and after (c).

Squeegee pressure, squeegee speed, snap off between screen and substrate, operation temperature and separation speed are some of the parameters used for the optimization of the printing quality. This process should be done in a climatically controlled room.

Disadvantage of this method is low aspect ratio. Cross section of a screen printed finger (line) on a substrate looks like the one shown in Figure 2.8 (a). To reduce the shadow effect, line width should be small. To reduce series resistance, the line cross section area should be high. For this reason, lines' height should be high while the width is small. However, it is usually not straightforward to obtain both conditions in the same system and in most cases, an optimum process condition is used.

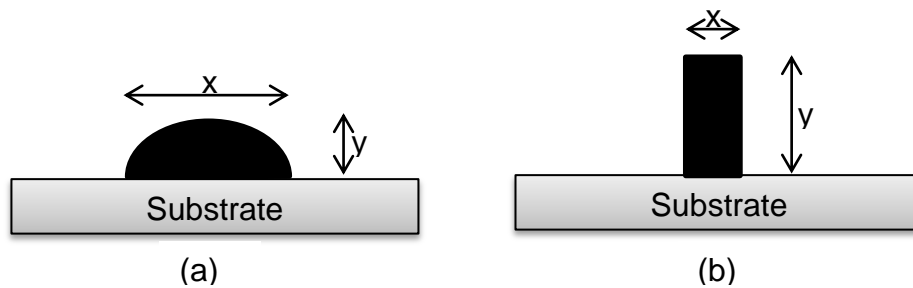


Figure 2.8 Cross sectional view of a screen printed line. (a) Realistic cross section. (b) Ideal cross section to reduce both series resistance and shadow effect.

Aspect ratio of a finger is the ratio between height of the finger and width of the finger. Average aspect ratio that can be obtained with screen printing is maximum 0.20-0.30 levels.

$$\text{Aspect ratio} = \frac{\text{height}}{\text{width}} = \frac{y}{x} \quad \text{Eqn. (2.6)}$$

2.3.1.2. Electroless Plating

Electroplating is a common method for semiconductor device fabrication. However, in mass production applications, electroless plating is more convenient. Contrary to the screen printing, electroless plating is a chemical method. Solar cells are dipped into a solution where a reduction reaction takes place. In this way, dissolved metals are plated on the surface of solar cell. Patterned plating is possible by scribing SiN layer by laser. Plating occur only on scribed Si surfaces, not on SiN surface.

This method is used for filling the grooves of buried contact solar cells. Buried contact solar cells provide high aspect ratios. By electroless plating method, silver and Ni/Cu plating can be done for front contact metallization.

Disadvantage of this method is the difficulties in the control of chemical reactions. Due to its low cost and good electrical resistivity, copper is preferred for plating applications. However, because of high diffusivity of copper, nickel layer is first plated under copper as a diffusion barrier. However pinholes in the Ni barrier may cause high copper diffusion through the junction causing loss of generated carriers.

2.3.2. Front Metallization

In metallization process, there is room especially for improvement for front metallization design. Different metallization patterns, metal contact formation styles and innovative approaches are available. In this section, some of these will be covered briefly.

a. Standard H-Bar design

H-Bar design is the most common design used in c-Si solar cells. As shown in Figure 2.9, it consists of fingers (thin lines) and busbars (thick lines). Number of fingers varies between 65 and 75, while number of busbars can be 2 or 3.

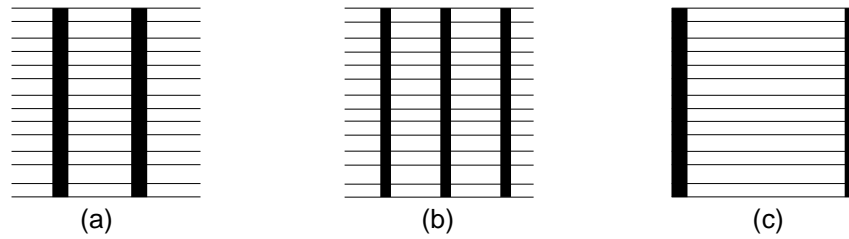


Figure 2.9 Different schematic versions of H-bar front contact designs. (a) Standard H-bar design with 2 busbars, (b) Standard H-Bar design with 3 busbars, (c) H-bar design with busbars at edges.

b. Metal Wrap Through design

Metal Wrap Through (MWT) structure doesn't include linear fingers or busbars on the front surface. Fingers and busbars in standard H-Bar design cover approximately 8% of the total cell surface. This covered surface blocks the light on metals and reduces the cell efficiency. Purpose of MWT design is to remove the busbars from front surface and thus increase the regions exposed to the sun radiation. In MWT design, the current collected by fingers are carried to back surface through the holes on the wafer. These holes are generally opened by laser pulses.

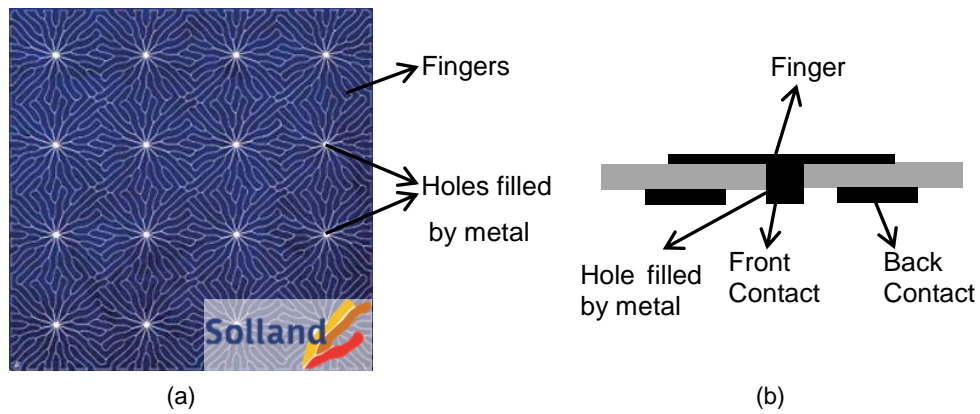


Figure 2.10 Metal Wrap Through Design, (a) Photograph of a MWT Solar Cell manufactured by Solland Solar [20]. (b) Schematic cross section view of a MWT Solar cell

As seen in Figure 2.10(a), there are no busbars in front of the solar cell. Fingers are not linear and optimized for minimum shadow effect. In Figure 2.10(b) it is shown that front metal contacts moved to back side through a hole on the wafer. Consequently, both negative and positive electrodes are on the back surface. This design provides a technical advantage for soldering the cell to each other during the module production. Furthermore, series resistance losses can be reduced in this approach.

c. Buried Contact Solar Cell (BCSC) design

As mentioned in Section 2.3.1.1, aspect ratio is the most important issue in finger printing. Thinner fingers improve the active surface area while increasing series and contact resistance. Buried contact design provides higher aspect ratios. BCSC includes a laser or mechanically opened grooves on the front surface under fingers and busbars as shown in Figure 2.11.

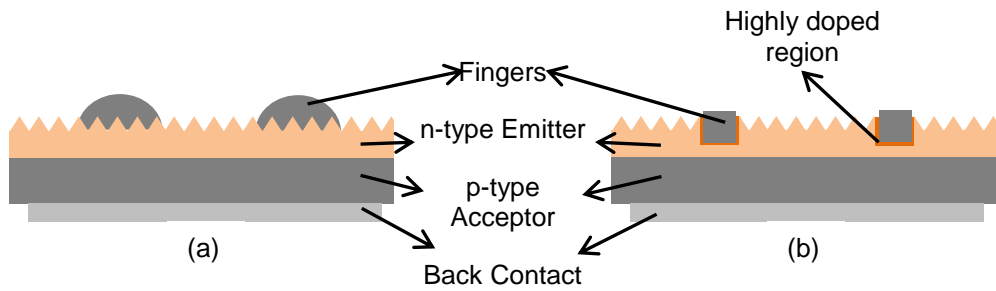


Figure 2.11 Schematics for (a) a standard screen printed solar cell cross-section and (b) buried contact solar cells cross-section

The aspect ratio of fingers in BCSC is higher than standard fingers. In addition, contact area between semiconductor and metal is larger, leading to a low contact resistance. Highly doped region under fingers add BCSC a selective emitter property.

Disadvantage of this design is the alignment procedure needed during the screen printing step. Unfilled volumes under metal may also cause recombination of carriers, which can be an important loss. For this reason electroless plating is chosen to form front contacts of BCSC.

2.3.2.1. Mathematical Description of the Metallization Pattern

There are two main loss mechanisms due to the front metallization: shadow losses and resistive losses. Antonius Radboud Burgers analyzed these loss parameters in his Ph.D. thesis [21] and optimized H-Bar grid pattern for test conditions and yearly yield.

Shadow losses: Front contact grid covers approximately 8% of the full cell areas both on 4" and 6" wafers. Fingers and busbars of this grid have definite length and width to reduce the contact resistance. The shadow loss due to the metal coverage can be calculated easily by considering the total area of fingers and busbars. As defined by Burgers, the parameters of the metallization is shown in Figure 2.12.

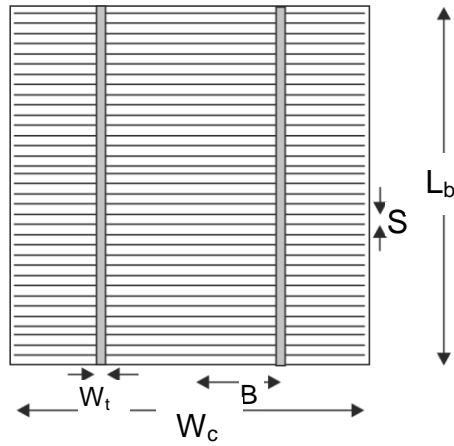


Figure 2.12 Dimensions of fingers and busbars on solar cell.

When the full metal contact area is calculated shadow loss due to busbars is:

$$\text{Shadow loss due to busbars} = p_{sb} = \frac{n_t(1 - t_b)W_t}{W_c} \quad \text{Eqn. (2.7)}$$

,while n_t is number of busbars, t_b is effective busbar transparency, W_t is busbar width and W_c is cell width. Shadow loss due to fingers is defined similarly:

$$\text{Shadow loss due to fingers} = p_{sf} = \frac{(1 - t_f)W_f}{S} \quad \text{Eqn. (2.8)}$$

,while t_f is effective finger transparency, W_f is finger width and S is finger distance. Therefore, total shadow loss is:

$$\text{Total Shadow loss} = p_{sb} + p_{sf} - p_{sb}p_{sf} \quad \text{Eqn. (2.9)}$$

Resistive Losses: Resistive losses result from the finger resistance, emitter resistance and contact resistance. There is a trade-off between resistive losses and shadow losses. When finger width increases, series resistance decreases while shadow loss increases. A balanced geometry should be optimized for the best efficiency. Martin Green formulized the resistive losses as described in Table 2.1.

Table 2.1: Resistive losses according to M. Green [22]

Loss in:	Total Loss (Ωm^2)
Finger	$\frac{B^2 S}{3} p_{lf}$
Emitter	$\frac{\rho_{s,l} S^2}{12}$
Tab	$\rho_{tt} \frac{2BL_b^2}{3}$
Contact	$\frac{\rho_c S}{W_f}$

2.3.2.2. Experimental Approach to Front Surface Metallization

Optimization of front surface metal contacts depends on process parameters and laboratory conditions such as doping concentration, printing screen, printing paste viscosity, firing tool, lab temperature, etc. Some of the requirements are hardly met with the present screen technology and available metal pastes. For instance, achieving high aspect ratio is the most important goal and the screen printing technique has limitations in reaching very high aspect ratios. Maintaining homogenous and continuous finger printing is another experimental challenge. As D.Erath et al. reported [23], fingers are not homogenous through the cell due to the inhomogeneous

mesh structure of the screen. As shown in Figure 2.13, finger height varies. The region with lower metallization causes high series resistance.

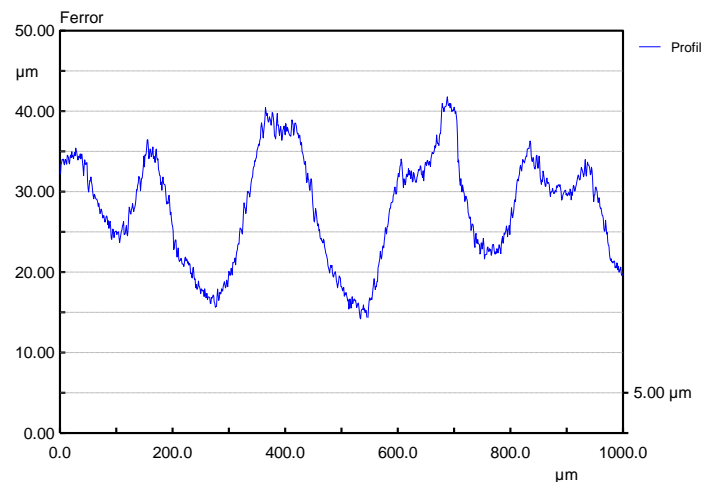


Figure 2. 13 Finger height profiles of GÜNAM cells measured in FERRO GmbH Labs

Gaps caused by broken Ag lines or defects on the surface are also important in collecting the generated carriers from the whole surface. Contamination in the metal paste or on the screen may result in the formation of the gaps in the finger lines. These gaps can be seen by eye or by electroluminescence systems. As shown in the Figure 2.14, points at which dark lines start, are the gaps of fingers. Since there is no contact to busbars, luminescence does not occur on these lines. Dark fingers can be assumed as not working.

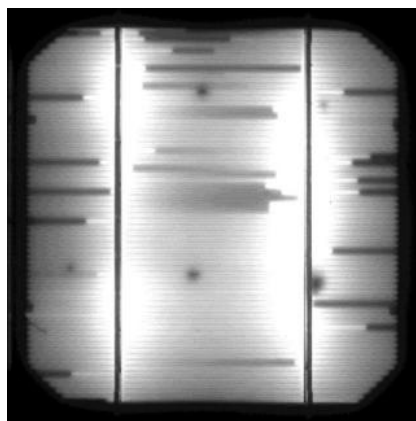


Figure 2.14 Electroluminescence image of a standard GUNAM Cell with 16% efficiency.

Another critical issue is the diffusion of Ag paste through the Si_3N_4 layer. Front surface of the solar cell is coated by nitrate. Between the nitrate and Si wafer there is another silicon-glass layer which is created during production steps. Front contact paste should diffuse through the silicon-nitrate and silicon-glass layers and reach the n-type region. On the other hand, too much diffusion will cause the Ag atoms to pass through the n-doped region and shorts the p-n junction. For this reason, the optimization is critical for the firing process. In the study reported by G.Schubert et al. [24], optimum firing temperature is given as 836°C with an IR belt furnace. However, in this study, a resistive furnace system was used, and therefore, all firing parameters such as peak temperature, temperature profiles of zones and belt speed were optimized. Another detailed research on firing parameters was done by T.Kwon [25].

In this study, printing optimization steps were extensively studied. As a part of the study, we collaborated with Ferro GmbH Labs in Hanau, Germany and visited their Lab in order to do simultaneous experiments. The details of the experiments conducted in Germany are discussed in Section 4.6.

2.3.3. Back Surface Metallization

Back surface metal contact printing is the simpler as compared to the front contact metalization. The most of the back surface is coated by Al paste to collect charge carriers. However, since Al is not a suitable material for soldering during module production, two busbars are separately printed on back side. These busbars are generally made from Al/Ag mixture or Ag paste. Busbars and some problematic points caused by firing furnace belt are shown in Figure 2.15.

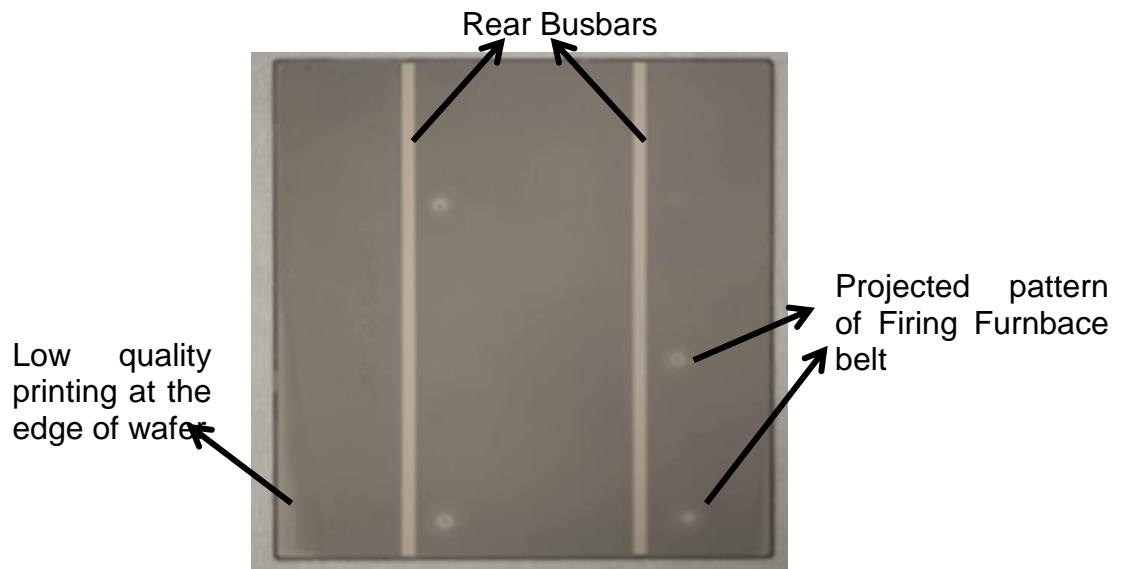


Figure 2. 15 Back surface metallization of a standard 6 inches c-Si solar cell.

Metallization with Al has several important functions on the back surface:

- I. Back Electrode: main function of the Al is to collect generated charges all over the surface. Since there is no light injection, the back surface is coated with Al.
- II. Removing the emitter surface on back side: Doping process is not selective. In doping furnace, both front and back surfaces are n-type doped. However, in solar cell design only front surface should be n-type emitter. For this reason n-type layer on the back side should be removed or converted to p-type. Since Al behaves as a p-type material, when it diffuses into the Si, this unwanted emitter layer vanishes.
- III. Back Surface Field: semiconductor-metal interface acts as an effective recombination region on the back surface. The photo-generated carriers recombine at the interface through the defect states. During the high temperature firing process, printed Al diffuses into the Si and creates a gradient of p-type region. This gradient creates an electric field (called back surface field) that pushes the minority carriers away from the interface, making the recombination less probable.
- IV. Back reflection: to get high energy conversion efficiency, all photons should be absorbed by the Si wafer. Although Si wafer is thicker than absorption depth of the light in silicon, some photons can still reach to back surface without being absorbed. Since Al is a good light reflector, all of these photons can be reflected back to the bulk Si. The back reflection increases the quantum efficiency of the solar cell.

There are several problems encountered during the metallization of the back surface of the wafers. First one is bump creation on the Al layer. After firing process at about 830⁰C, bumps on the surface can be observed. This problem depends on the paste's bump resistance and temperature profile of firing furnace. Details of this problem are studied by S.Park [26]. Another

issue is the homogeneity of the Al layer printed over a large area. An example of the problem can be seen on Figure 2.15.

CHAPTER 3

EXPERIMENTAL PROCEDURES

3.1. Metallization System (Screen Printing)

3.1.1. Screen printer

Screen printing is the most common technique for metallization of solar cells. The basic principle of the technique is explained in section 2.3.1.1. During this study a lab type screen printer manufactured by ASYS was used in GUNAM laboratories. The printer is an ASYS X1 SL model screen printer with manual load and unload, which is also compatible with different size wafers and adjustable printing parameters.



Figure 3.1 a) Photograph of screen printer used in this work, b) snapshot of the system software

The system operation is fully computer controlled. A snapshot of the printer software is shown in Figure 3.1b. Since the critical processes of the solar cell production are already completed at this point, the metallization process does not require a clean room environment.

Screen printing is very important for the fabrication of high efficiency solar cells. The quality of the printed metal contacts depends on several parameters such as printing speed, printing pressure, snap off etc. These parameters are:

- *Squeegee Speed*: Squeegee is the rubber apparatus, which swaps the metal paste on the screen. Speed of the squeegee is the most important factor for the quality of the printing. Speed can be adjusted between 0-200 mm/s.
- *Squeegee pressure*: Squeegee applies a pressure onto the screen for the diffusion of the paste through the screen. This pressure can be adjusted between 0-4 bars with our instrument.
- *Snap off*: Wafer and the screen are not in contact position during printing. There is a gap between them and this gap is called snap off. (See Figure 3.2) This parameter is important to determine the amount of paste which will be diffused. Snap off can be adjusted between 0-5 mm.
- *Separation Speed*: After printing the paste, metal fills the gap between screen and wafer. Since the paste is still in aqueous form in this step, separation speed is important to keep paste homogenous.

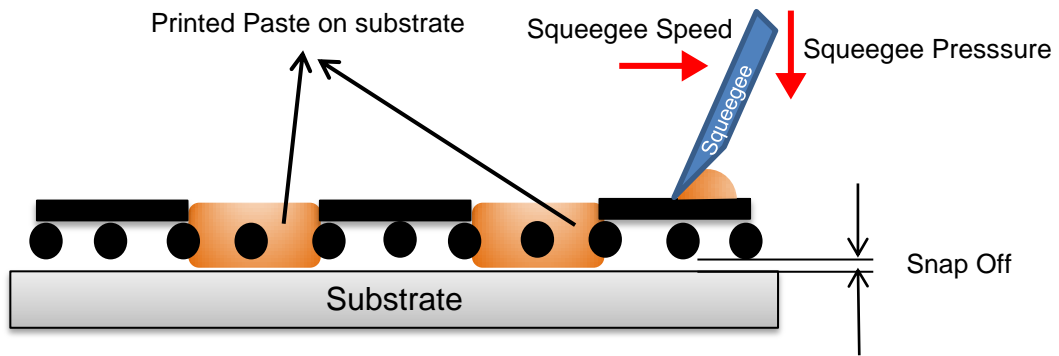


Figure 3.2 Schematic showing squeegee pressure, squeegee speed and snap off

3.1.2. Metallization Masks

We have designed the printer masks using a drawing program and manufactured them at by SSF Company [27]. Generally different masks are used for a standard solar cell metallization. The metallization process is as follows: first mask is used for back surface busbars. It consists of parallel busbars formed by Ag or Ag/Al mix pastes. The purpose of these busbars is to enable us to solder wires to the back contact of the cell. This will make it possible to connect cells to each other. The second mask is to cover the most of the back surface area with Al paste. Since total printing area is very large for the Al metallization, homogeneity is very important in this step. Final mask is the front contact metallization mask. It is used to form 65-75 fingers and 2-3 busbars with Ag paste. Schematic of all these screens are shown in Figure 3.3. A photograph of a mesh with emulsion is given in Figure 3.4.

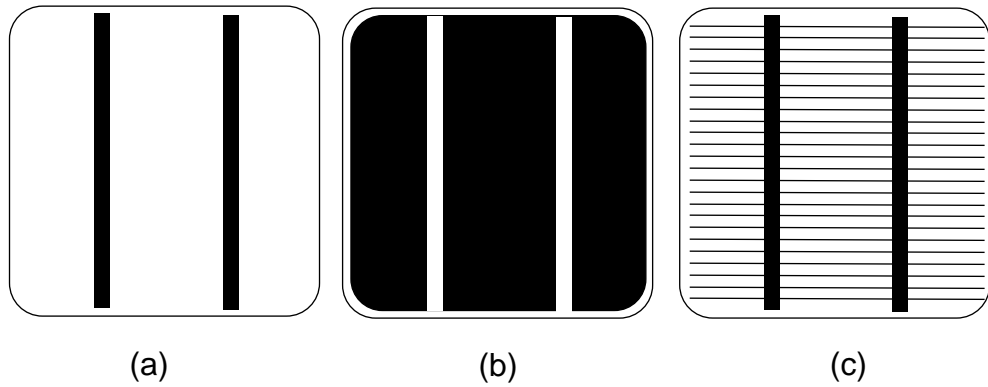


Figure 3.3 a) Back busbar mask, b) back aluminum mask, c) front Ag Mask.
Black areas are mesh openings

In addition to mask opening designs, masks' mesh parameters are also changing. Variable parameters are mesh count (number of wires per inch), wire diameter, emulsion thickness, tension, tension angle and photo plot resolution. The mesh parameters of the masks that are used in this study are given below:

Table 3.1 Properties of masks which are used in this study.

Mask	Mesh Count	Wire Diameter [μm]	Emulsion Thickness [μm]	Tension [N/cm]	Tension Angel [degree]	Plot Resolution [dpi]
Back Silver	200	40	5±2	28±2	22,5	10000
Back Aluminum	200	40	5±2	28±2	22,5	10000
Front Silver	280	25	15±2	28±2	22,5	16000

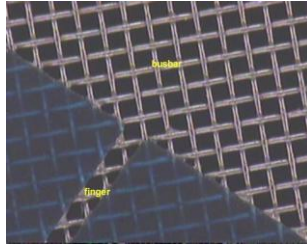


Figure 3.4 Sample image of a screen printing mesh [28].

3.1.3. Metallization Pastes

Producing the paste form of a metal is a special process and it is out of the scope of this thesis. Al paste, Ag paste and Ag/Al mix pastes with different viscosities are being used in the solar industry. Generally, each product has its own data sheet that includes firing recipes. Throughout this study, we have developed some key methods to use with these pastes.

- Conservation of paste solvents: Pastes include metal molecules, resin and some other solvents. These resin and solvents are volatile at room temperature. To keep these resin and solvents stable, pastes should be stored in a closed container immediately after printing and the lid of the box should be sealed with electrical tape.
- Homogeneity of the pastes: Especially in university labs, pastes may wait for a long time between each process. Therefore, separation of solvents and the metal can be seen. When this happens typically the metal particles precipitate to the bottom. To avoid precipitation, pastes should be stirred on a roller over night before the printing process.
- Room air conditioning: Optimum room temperature is about 20-25⁰C for screen printing. Higher temperatures may cause evaporation of the resin and solvents of pastes while it is on screen. Especially Ag pastes are very sensitive to ambient temperature. If any paste dries on the screen, it blocks the mesh openings and that causes printing failure.

In this study pastes from Ferro GmbH are used. These pastes are PS 2130 for back Silver, NS 3116 for front silver and AL 5130 for back Aluminum.

Ingredients of these pastes are characterized with Electron Dispersive X-Ray (EDX). According to EDX results, Al paste include C, O, Al, Si, K, Ti and Co while silver paste include C, O, Mg, Ag, K, Fe and Pb. It is known that there are some organic and inorganic volatile compounds in the pastes. It is hard to detect polymers in the pastes. Generally they are commercial secrets. Only effect of the firing to the pastes is observed with EDX analysis. Details of the test will be given in section 4.5.

3.1.4. Drying Furnace

Pastes reach their final solid phase after firing. However, all 3 printing steps should be done before the firing. To keep printed paste on the wafer without any damage during successive printing processes, a simple drying step after each printing should be applied. This step does not require high temperature. IR belt furnace or box type furnaces can be used for this process. In this study, we have used a box type furnace made in Turkey. It is capable of heating up to 250°C. There is a fan inside the furnace to obtain homogeneous heat distribution and an exhaust to remove evaporated solvents from the paste.

3.1.5. Firing Furnace

Firing is the most important and critical step of metallization process. There are several functions of this step such as metal solidification, back surface field creation and metal diffusion into the emitter layer. Details of these functions are described in Section 2.3. The key point about the firing is that the wafer temperature should rise to 850-950°C very rapidly and followed by a rapid cooling down to room temperature. This kind of rapid heating and

cooling is not possible with standard tube or box furnaces. Therefore, belt furnaces with at least 3-4 heating zones are used for the firing process. The furnace, which we have used in this study, has 7 heating zones. Belt speed can be adjusted for each zone and the position of the wafers can be monitored by a computer.

All metallization pastes have their own firing temperature profiles described in their datasheets. An example of sample firing temperature profile is given in Figure 3.5. However, these temperatures may not be applicable to all cases because the performance depends on other parameters like process room conditions etc. For example, generally solar cell firing furnaces use IR heaters since control of IR heaters is easier than the resistive heaters. Moreover, IR heaters heat the wafers by radiation not by convection, so energy per square meter is constant in IR heaters. In our lab, we used a resistive furnace shown in Figure 3.6. As a consequence, we had to optimize all firing parameters from the beginning.

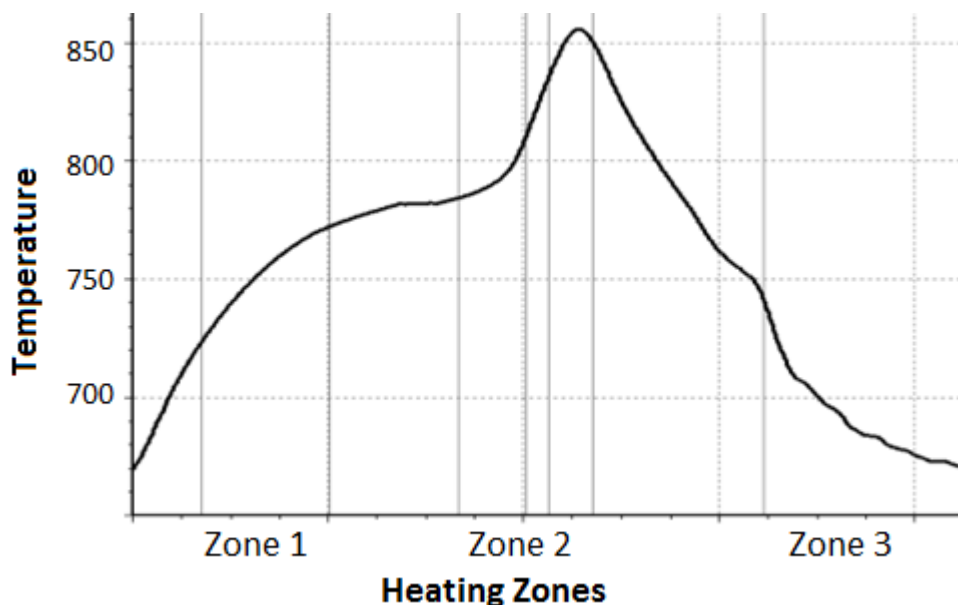


Figure 3.5 Recommended sample firing temperature profile [29]



Figure 3.6 a) Photograph of firing furnace used in this study and b) a snapshot of the control software.

3.1.6. Solar Simulator

Electrical characterizations of the cells were done with a solar simulator manufactured by QuickSun. It is a flash lamp simulator, which is calibrated to A.M. 1.5 conditions. We can measure 4 inch and 6 inch solar cells with 2 and 3 busbars. Fully computer controlled simulator gives most of the electrical properties discussed in Section 2.1. Simulator makes self-calibration with its internal reference solar cell and makes temperature correction according to the room temperature. Photograph of the simulator and snapshot of the software can be seen in figure 3.7

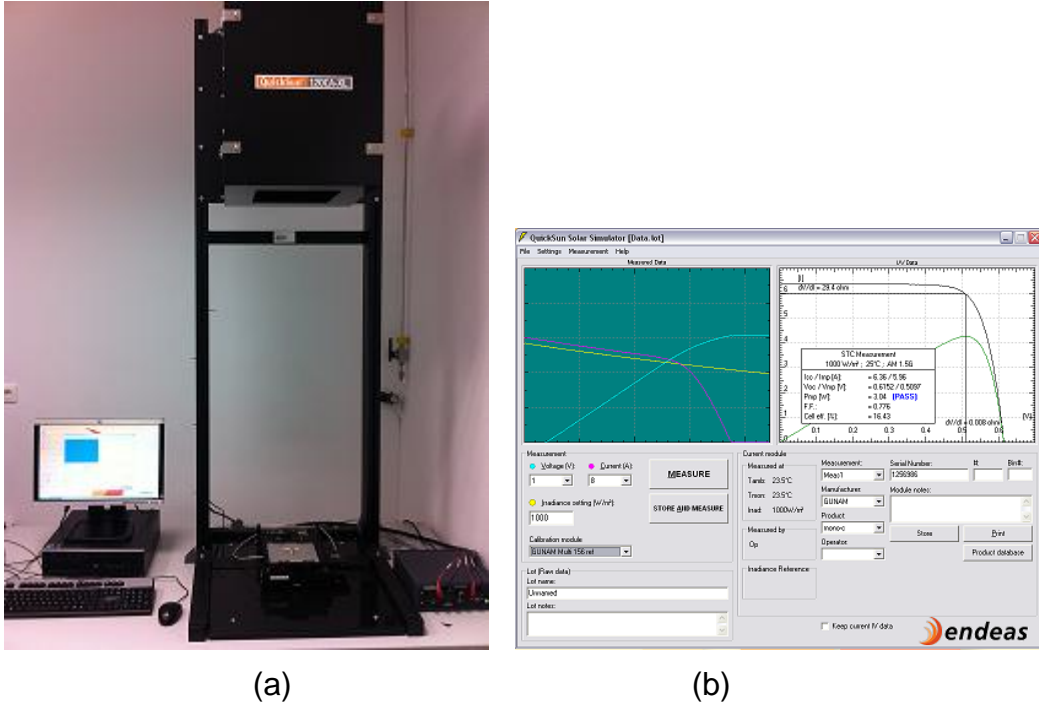


Figure 3.7 Photograph of solar simulator and snapshot of the simulator software

3.2. Contact Resistance Measurements

At the beginning of the metallization optimization study, contact resistance measurements were done with both Al and Ag pastes. Details of the theory of contact resistance measurement methods are given in several graduate studies [30] [31]. Although other approaches are possible, Transmission Line Method (TLM) is usually chosen to determine contact resistance between metal and semiconductor. The contact resistance between a metal layer and the underlying substrate is given by

$$R_c = \frac{\rho_c R_{sheet}}{L} \text{ if } d \gg \lambda \quad \text{Eqn. 3.1}$$

, where R_{sheet} is resistance of the semiconductor, ρ_c is contact resistivity, L is width of the metal contact, d is distance and λ is penetration length [32].

In the TLM method, the contact resistance is derived from the relation between measured different resistances from different lengths. TLM pattern can be seen in Figure 3.8. All data taken from the pattern sketch on the graph and extrapolated curve gave the twice of the contact resistance where the curve intersect with y axis. A sample graph is given in Figure 3.8.

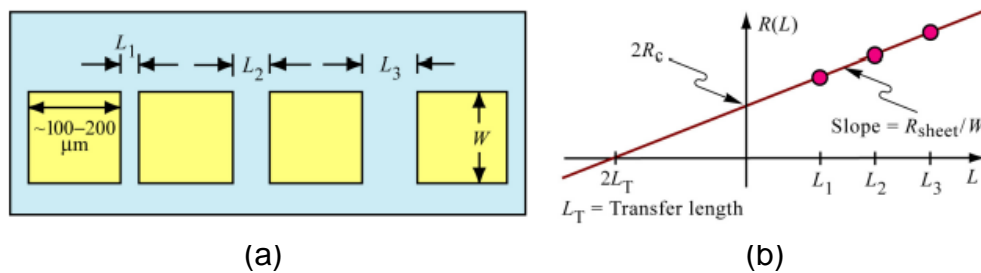
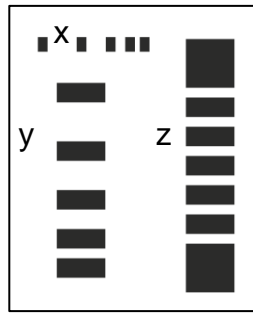


Figure 3.8 a) Contact geometry and b) Sample TLM Graph [32]

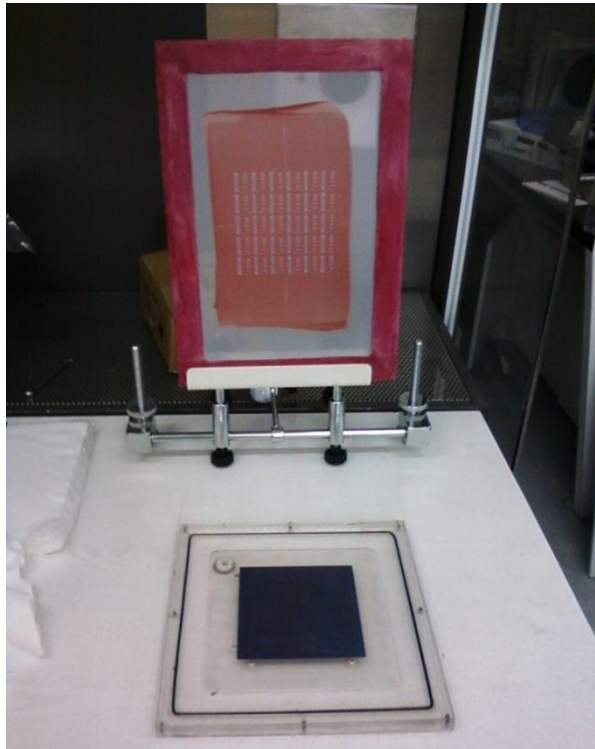
To make TLM pattern on Si wafers, screen printing method is applied in order to study the case for standard solar cell process. We designed and produced manual screen printing mask and manual printing setup for this purpose. As shown in Figure 3.9, three different TLM patterns were designed and a screen printing mask, which includes 30 copies of the pattern was prepared. The purpose of multi-patterned mask is printing many patterns on 6 inches wafers. Designed patterns and prepared mask can be seen in Figure 3.9 a and b respectively. By comparison, it is seen that pattern X and Y give the same contact resistance value. Since pattern Z is too small, result of this pattern is not reliable. We decided to do all measurement with pattern X.



(a)



(b)



(c)

Figure 3.9 Contact resistance measurement used in this work. a) TLM pattern, b) manual screen printing mask and c) manual screen printing setup

CHAPTER 4

OPTIMIZATION OF FRONT&BACK SURFACE METALLIZATION OF c-Si SOLAR CELLS BY SCREEN PRINTING

4.1. Introduction

Throughout this study, many test samples were prepared and measured. They were prepared by standard solar cell production methods, which include saw damage etching, surface texturing, doping and anti-reflection layer (Si_3N_4) coating. Details of these processes can be found in the previous graduate study carried out at GÜNAM [19]. In this work we have studied all aspects of the screen printing based metallization process.

4.2. Contact Resistance

Contact resistance between a metal layer and the underlying substrate is found from the expression given by equation 3.1 in previous chapter. Variables that can affect the contact resistance are drying temperature, drying time, firing temperature and firing furnace belt speed. After drying and firing processes, samples were measured by four-point probe method.

4.2.1. Dependence of Contact Resistance on Drying Process

Al and Ag pastes were studied with different drying temperatures and drying times. The contact resistance results are shown in Figure 4.1. Data displayed in these figures represent an average of 5 different measurements. All samples were fired under 850⁰C with 100 mm/s conveyor speed. Since firing process was not optimized in this step, these firing parameters were chosen arbitrarily.

We see that the resistance values are very low as desired with a small variation.

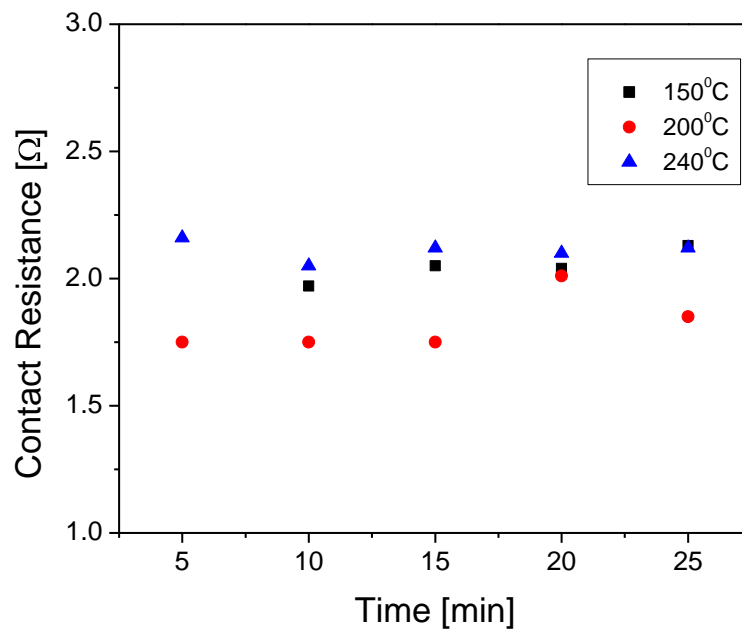


Figure 4.1 Contact resistance of Al paste on Si wafer as a function drying temperature and time.

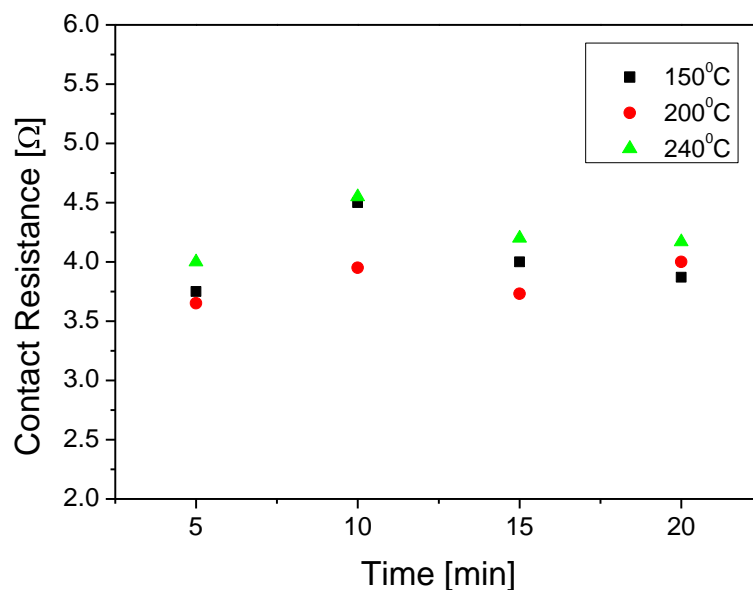


Figure 4.2 Contact resistance of Ag paste on Si wafer as a function of drying temperature and time

From this result, we can conclude that the temperature and the duration of the drying process have minor effects on the contact resistance values.

We must however note that excessive drying might cause over evaporation of solvents from the paste that can result in problems during the firing process. Based on these observations, we have concluded that 5 minute drying is enough for both Al and Ag pastes.

4.2.2. Dependence of Contact Resistance on Firing Process

Most of the pastes have their own firing recipe for a standard firing furnace. Since our firing furnace is not a standard furnace, we optimized all firing parameters thoroughly. Firing parameters such as firing profile and conveyor speed might affect electrical properties of the metal layer and its contact

resistance with the underlying layer. Details of firing optimization are explained in Section 4.5. In this step, only contact resistance is presented with respect to firing furnace parameters. Three different firing temperatures and conveyor speeds were tested to observe the contact resistance dependence.

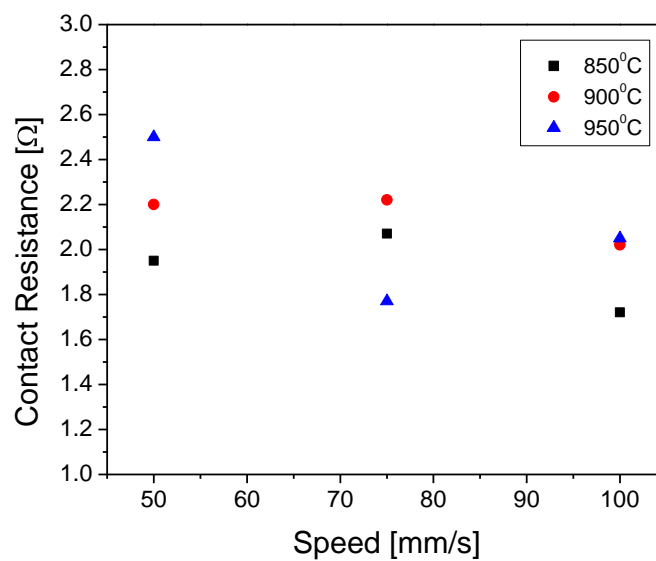


Figure 4.3 Contact resistance of Al paste on Si wafer as a function of firing temperature and speed

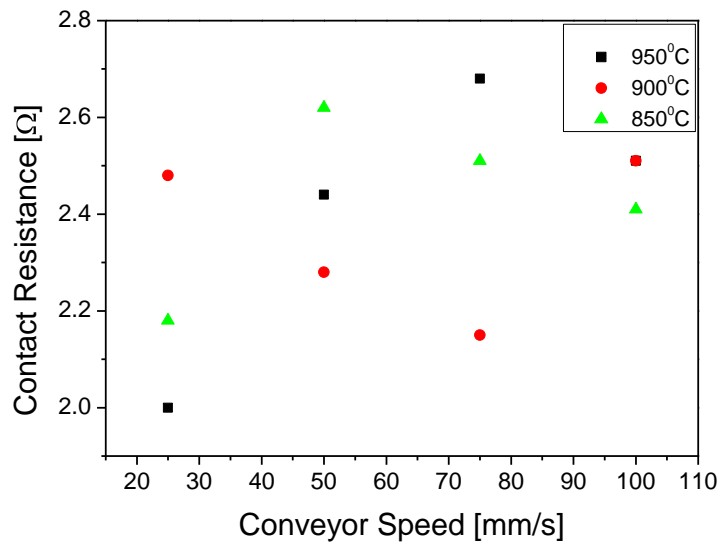


Figure 4.4 Contact Resistance of Ag paste on Si wafer as a function of firing temperature and time

Again the effect of firing on the contact resistance is minimal. Although lower temperatures and higher conveyor speeds seem to be giving low contact resistance, the variation is not significant to draw conclusion on this effect. The contact resistance measurements provided a starting point to optimize metallization.

4.3. Front Surface Metallization

Screen printing parameters are very important for front contact metallization. Hardness of printed thin fingers, homogeneity of the height and the width of the fingers and the aspect ratio are critical for a reproducible and reliable metallization process. Squeegee speed, squeegee pressure, snap off and separation speed are the computer controlled parameters. Descriptions of these parameters are given in Section 3.1.1.

4.3.1. Squeegee Speed

Squeegee speed can be set from 1 mm/s to 200 mm/s with our equipment. For industrial applications, 200 mm/s is preferable to achieve high throughput in the production line. In this study, 6 different speeds between 20-200 mm/s were compared for finger width and heights as measured by a surface profilometer (Dek-Tak). Each sample was measured from 5 different points and averages were taken. Results can be seen in Tables 4.1, 4.2 and Figures 4.5, 4.6, 4.7. All pastes printed on wafers were dried for 5 minutes at 200°C and fired under 850°C with 100mm/s conveyor speed.

Table 4.1 Finger height and width data taken from points A,B,C and D

Squee. Speed [mm/s]	Width A [μm]	Height A [μm]	Width B [μm]	Height B [μm]	Width C [μm]	Height C [μm]	Width D [μm]	Height D [μm]
25	141	20	133	27	141	26	129	33
50	134	23	138	27	136	25	139	30
75	130	25	130	20	134	29	134	30
100	134	29	126	28	128	21	130	21
150	128	22	123	18	130	25	130	26
200	130	32	130	31	129	31	132	33

Table 4.2 Average Finger dimensions with respect to Squeegee Speed.

Squeegee Speed [mm/s]	Height deviation [μm]	Average Width [μm]	Average Height [μm]	Aspect Ratio
25	14	135.2	26.4	0.19527
50	16	136.6	25.8	0.18887
75	15	132.4	25.8	0.19486
100	16	129.6	26.2	0.20216
150	13	129.4	24.8	0.19165
200	13	128.8	32.6	0.25311

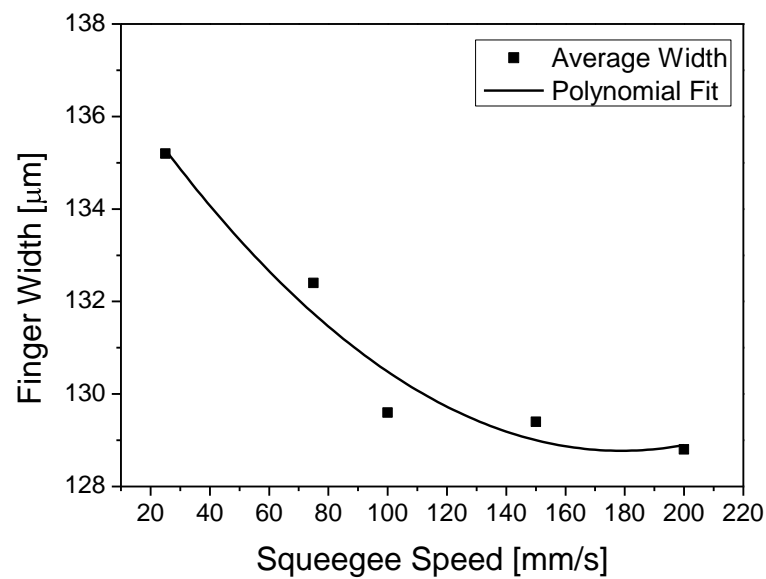


Figure 4.5 Squeegee speed dependence of average finger width.

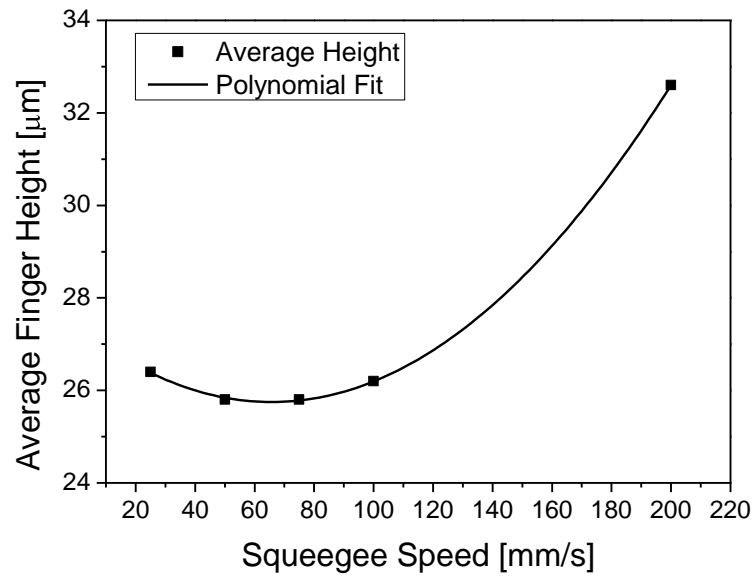


Figure 4.6 Squeeze speed dependence of average finger height.

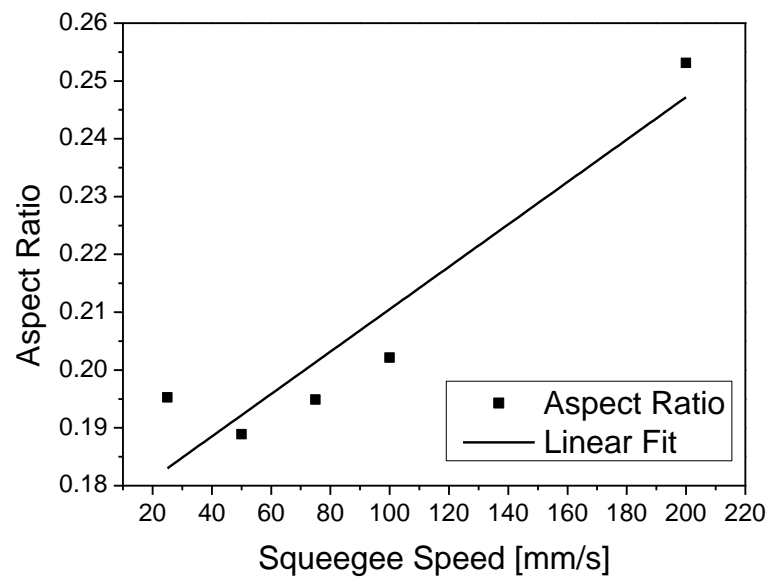


Figure 4.7 Squeeze Speed dependence of average aspect ratio.

As seen in the graphs displayed in Figures 4.5 and 4.6, increasing squeegee speed increases the finger height and decreases the finger width as expected. 25% aspect ratio was achieved with the highest squeegee speed. This aspect ratio is a standard value, which is acceptable for all production lines [33]. After this point, in all experiments squeegee speed was chosen to be 200mm/s.

4.3.2. Squeegee Pressure

Pressure of the squeegee is another important parameter for screen printing since the diffusion of the paste through the mask depends directly on the squeegee pressure. In this part, squeegee speed, drying and firing parameters were chosen according to the previous experiments. 10 different squeegee pressure values were tested between 0.2 and 3.5 bars. Finger heights and widths were measured by surface profilometer (Dek-Tak) from 5 different points of the same sample. Average values are given Table 4.3. As seen in Figures 4.8, 4.9 and 4.10 the results are similar; but, the observed trend can be summarized that the aspect ratio decreases with increasing squeegee pressure.

Table 4.3 Average Finger dimensions with respect to Squeegee Pressure.

Squeegee Pressure [Bar]	Average Width [Microns]	Average Height [Microns]	Aspect Ratio
0.2	119.8	28.4	0.2370
0.5	123.4	28.8	0.2333
0.8	128.8	29	0.2251
1.0	124.6	28.8	0.2311
1.3	125	30.6	0.2448
1.5	131.8	28.4	0.2154
2.0	129.4	27.4	0.2117
2.5	128.6	25.2	0.1959
3.0	132.4	28.6	0.2160
3.5	126.8	26.6	0.2097

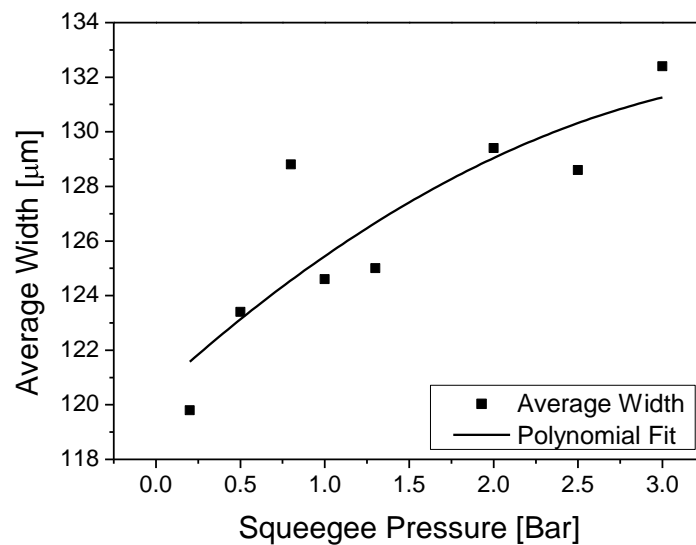


Figure 4.8 Plot of average finger widths vs. squeegee pressure.

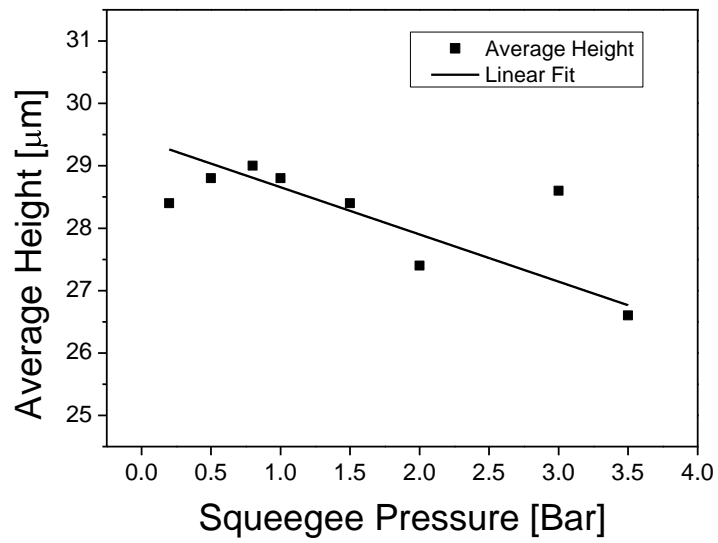


Figure 4.9 Plot of average finger heights vs. squeegee pressure.

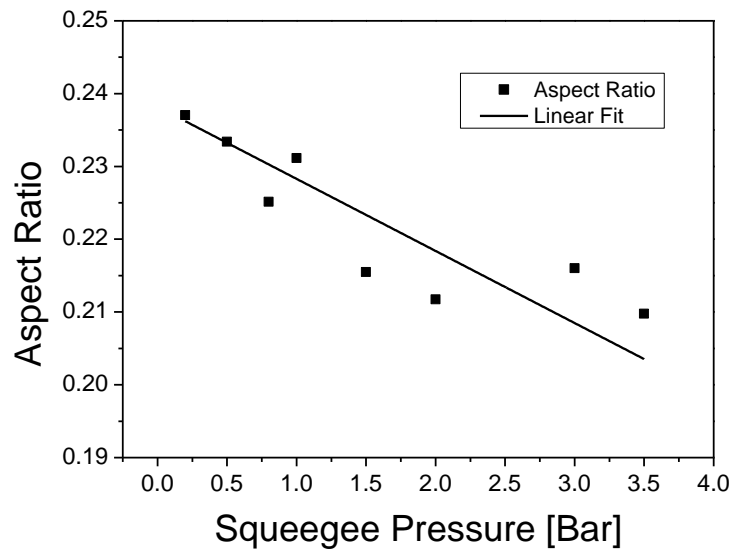


Figure 4.10 Plot of aspect ratio vs. squeegee pressure.

As expected, finger width increases while the average height decreases with pressure. Consequently, aspect ratio decreases with the squeegee pressure. In the rest of our study, 1.3 bars squeegee pressure was chosen as optimum squeegee pressure. In all the following experiments, squeegee pressure was set to 1.3 bars.

4.3.3. Snap Off

Snap off is the distance between printing mask and wafer. This distance determines the remaining paste level after squeegee sweep all the wafer. When the squeegee applies a force on the mask, mask bends downward and this distance vanishes. If the snap off is too high, mask cannot bend enough and paste cannot touch the wafer. For this reason snap off should be very low. In this experiment, 6 different snap off values were tested between 0.1 and 0.6 mm, and the results are shown in Figures 4.11, 4.12 and 4.13.

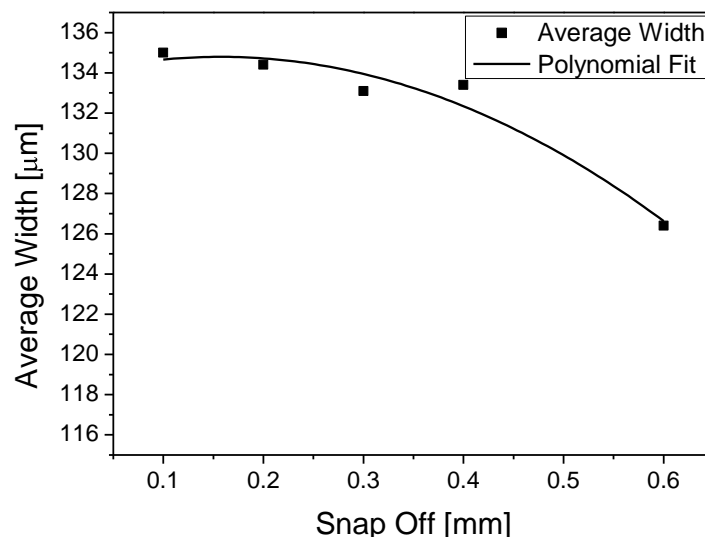


Figure 4.11 Plot of average finger widths vs. snap off.

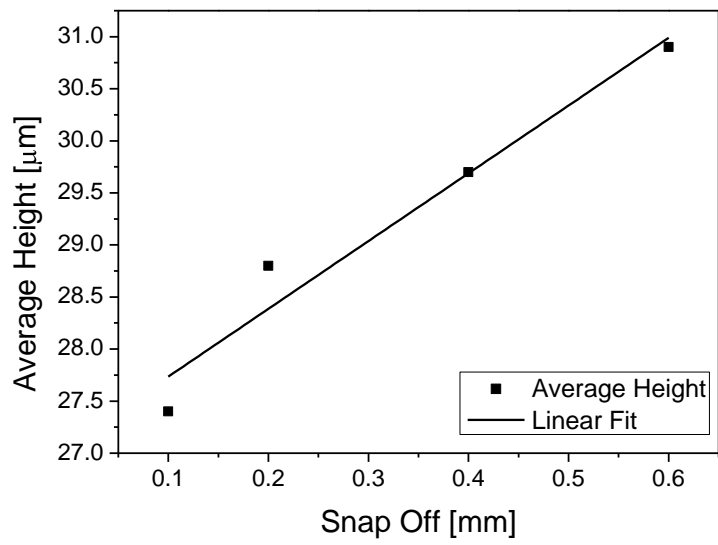


Figure 4.12 Plots of average finger heights vs. snap off.

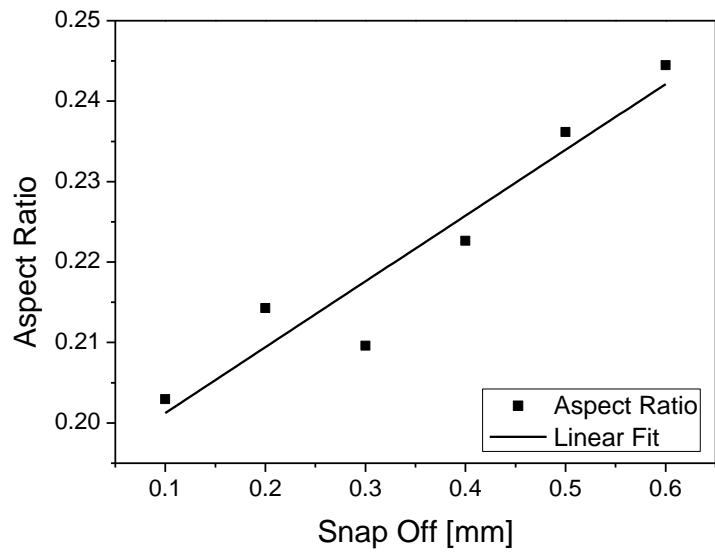


Figure 4.13 Plots of aspect ratio vs. snap off.

Since the geometry of the finger depends on the gap between mask and wafer, aspect ratio is very sensitive to the snap off value. Increasing snap off enhances the aspect ratio. In the present study, it increased from 20% to 24.5% by optimizing the snap off. According to the results shown in Figure 4.13, it seems to be possible to increase the aspect ratio by higher snap off values than 0.6. However, when the snap off values are too high, the mask cannot bend enough and paste does not touch to the wafer. Therefore, 0.6 mm is the max snap off for our equipment and samples.

4.3.4. System Stability Test

After optimization of main printing parameters prior to the firing optimization, we decided to test the reliability of the system. For this test, we prepared 10 pieces of 6" full wafer samples and printed with the same optimized parameters. Each sample measured from 2 different points and average data were evaluated.

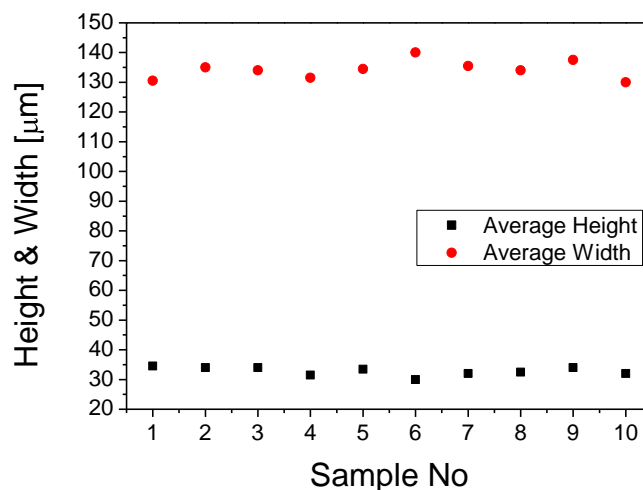


Figure 4.14 Finger height and widths of the samples, which printed with same parameters.

During these experiments squeegee speed was 200 mm/s, squeegee pressure was 1.3 bars and snap off was 0.6 mm as optimized, firing temperature was 870°C and conveyor speed was 100 mm/s as suggested by the paste producer company. Results shown in Figure 4.14 seem acceptable since all finger heights and the finger widths are close to each other. By this experiment it is seen that printing system is reliable.

4.3.5. Finger Homogeneity Test

Another important point about the geometry of fingers is homogeneity of the finger from one end to busbar. Height profile of the finger was measured by a surface profilometer with a good alignment as shown in Figure 4.15. Scanning length was 2 mm. Difference between the minimum and maximum point of the height is called as “height deviation”. Parameters which are compared in this experiment and height deviation results are given in Table 4.4.

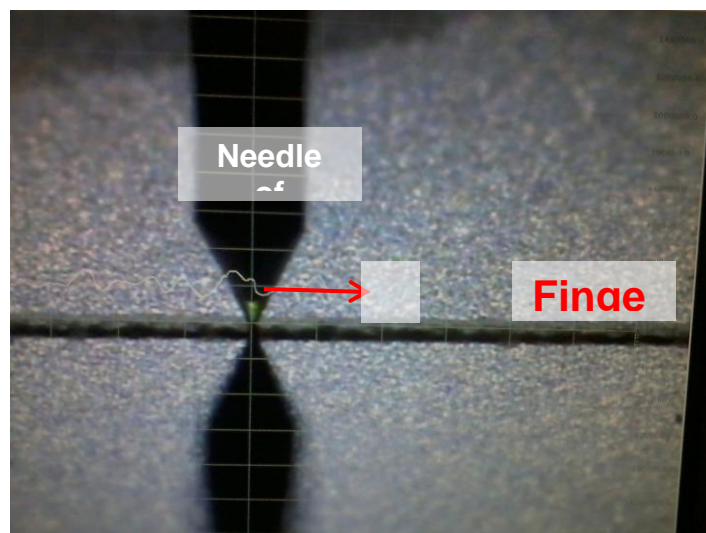


Figure 4.15 Finger homogeneity test method by Dek-Tak Profilometer.

Table 4.4 Height Deviation depending on printing parameters.

Sample No	Squeegee Speed mm/s	Squeegee Pressure bar	Seperation Speed mm/s	Snap Off mm	Height Deviation microns
1	150	1	5	1	NA
2	150	4	5	1	28
3	150	1	5	0.6	17
4	150	3	5	0.6	11
5	150	1	5	0.5	14
6	150	1	5	0.4	15
7	150	1	5	0.3	17
8	150	1	5	0.2	14
9	150	1	5	0.1	15
10	150	4	5	0.1	14
11	150	1	5	0	15
12	150	4	5	0	14

According to Table 4.4, deviation can be reduced by changing squeegee pressure and snap off. Minimum deviation, which can be achieved, is 11 microns. Since there is no data about it in the literature to compare, we measured a commercial solar cell's (Big Sun Energy Technology Inc. [34]) finger height deviation. Result was 13 μm . So, 11 or 14 micron deviation seems to be acceptable for industrial applications. Moreover, we observed a periodicity in the height profile, as shown in Figure 4.16.

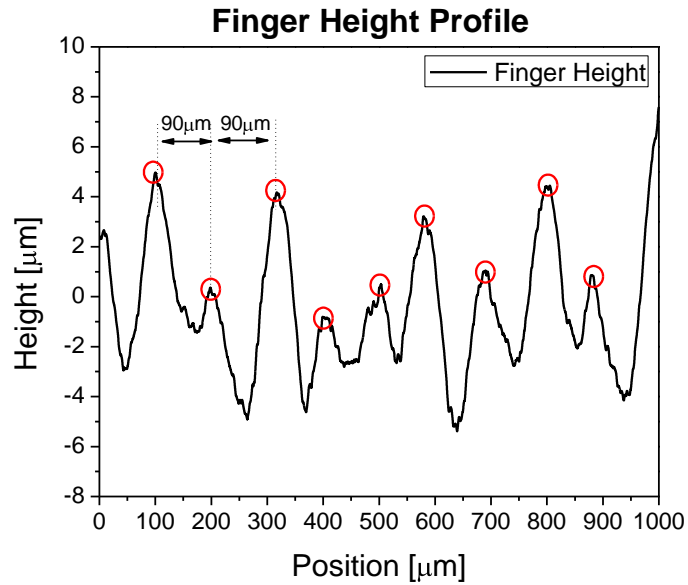


Figure 4.16 Surface profile of a finger

When distances between the peaks are measured, they are exactly 90 microns that is same the distance between openings of the printing masks. So, this periodicity in the profile is just the projection of the mask mesh. Similar results were also reported by Birger Retterstøl Olaisen et. al. in their publication [35].

Consequently, with this experiment we found an acceptable height deviation and understood the reason for the height variations. More results on this point can be found in Section 4.6.

4.4. Back Surface Metallization

As mentioned above, back surface metallization consists of 2 different printing steps: first one is back busbar printing with Ag and the second one is covering the remaining part of the surface with Al printing. Back busbars are necessary for the soldering of cells to each other during solar module

production. However, since our samples wouldn't be used for module production, we omitted the back busbars and prepared a full back surface Al printing mask by modification of standard back surface Al mask. Photographs of modified mask can be seen in Figure 4.17.

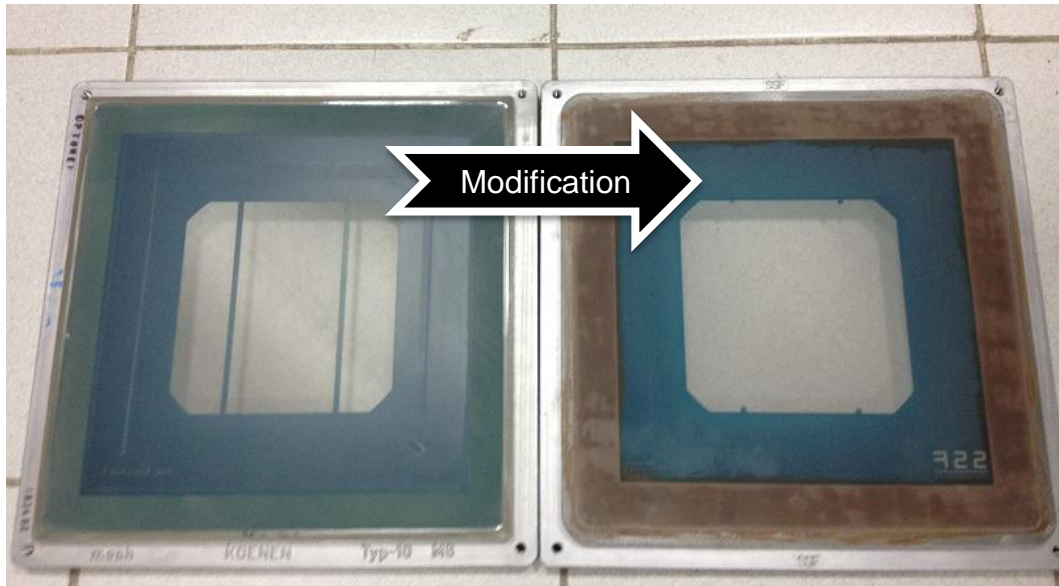


Figure 4.17 Photograph of conventional & modified of back Al masks.

Since the back surface metallization does not include fingers, there is no need for aspect ratio or thickness optimization on the back side. During the metallization of the back surface the Al film on the wafer should be homogenous. If Al thick film is not homogeneous, during firing process, thermal stress cause “lift off” of the Al. In Figure 4.18 photographs from lifted of samples can be seen.

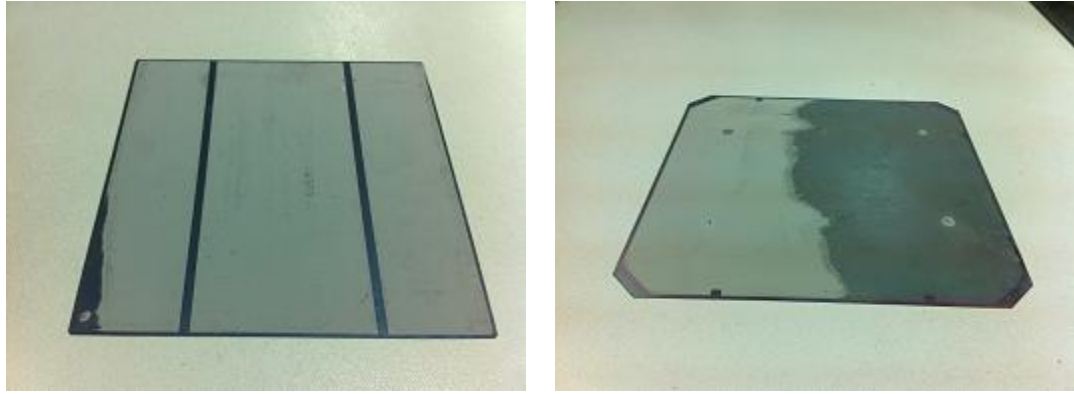


Figure 4.18 Non-homogeneity problem of Al contact.

The reason for this problem is the non-homogeneity in bending of the mask when the squeegee applies pressure on it. As a solution, snap off was set to zero and squeegee pressure was reduced to 0.6 bars.

Another problem about printing was the sticking of the printed metal layer onto the surface. Since printing area is too large, Al paste acts as glue and after printing, wafer sticks under the mask. Although there is a vacuum chuck system that keeps the wafer on it, when separation speed is standard, wafer got stuck on the mask. Reducing the separation speed easily solved the problem.

Another optimization parameter about back surface metallization is the amount of the Al paste printed on the wafer. Although it is not important functionally, it is important for the cost of a single cell. In this study squeegee pressure, squeegee speed and snap off dependence of the Al mass was tested.

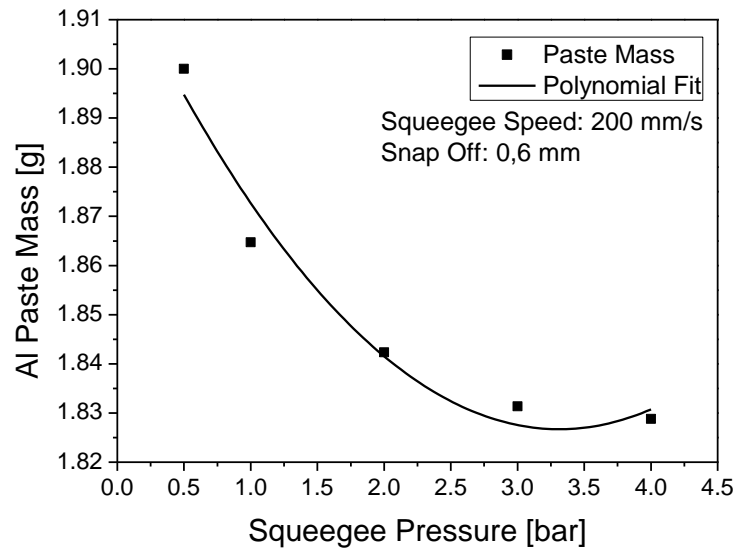


Figure 4.19 Squeegee pressure dependence of Al metal paste mass.

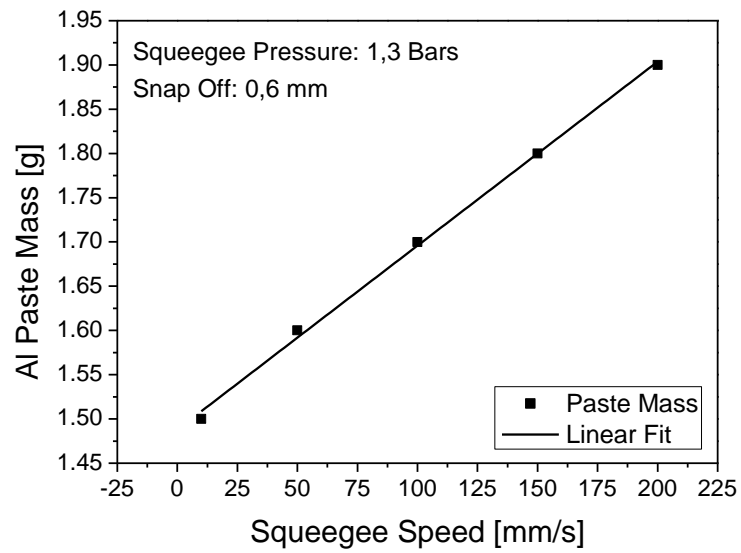


Figure 4.20 Squeegee speed dependence of Al metal paste mass.

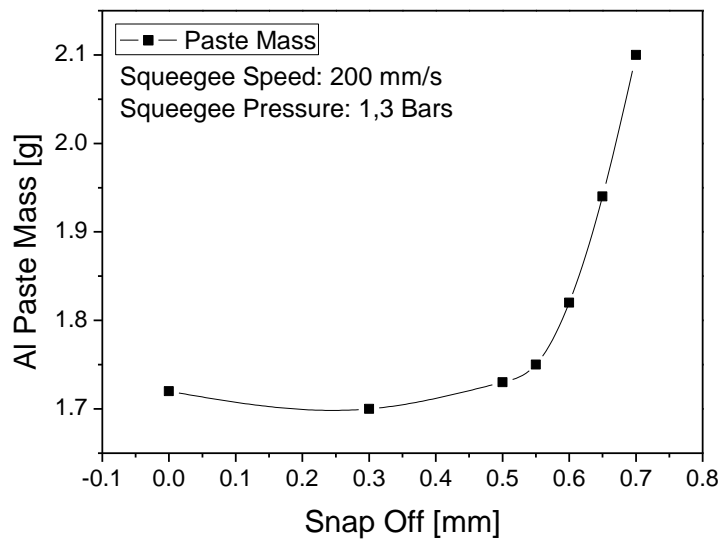


Figure 4.21 Snap off dependence of Al metal paste mass.

We see that Al paste mass depends on the squeegee speed and inversely proportional to the squeegee pressure. Snap off dependence seems to be exponential.

4.5. Firing Optimization

Firing is the most critical part of the metallization process. Solar cells should be heated up rapidly and kept at high temperatures for less than 1-2 seconds and cool down rapidly. This kind of temperature profile cannot be supplied in a standard box or tube furnaces. For this reason, conveyor furnaces with IR heaters are used for this application. Generally these furnaces have 3 or 4 heating zones and heater accuracy is 0.1 Celsius degrees. However, our furnace is a seven zone system with resistive heaters whose accuracy is ± 5 Celsius degrees. Firing optimization study included several samples and

parameters. During optimization studies, we have changed the metallization paste and we had to repeat the optimization study.

As mentioned in Section 2.3, firing steps have several functions such as removing resins in the pastes, back surface field creation and silver diffusion into emitter layer. To compare the overall results of the all these physical phenomena, I-V characteristics of the fabricated solar cells were used as the characterization method.

4.5.1. Firing Optimization Experiments

Variable parameters of the firing furnace are heating zone temperatures and conveyor speed. In order to fully understand the firing process 5 main experiments were performed:

Experiment 1: In this experiment paste A was used to compare different conveyor speeds. Conveyor speed is separated as “entrance speed” to the furnace and “hot zone speed”. 3 different experiment sets were tested.

Experiment 2: According to the results of experiment 1, we have performed second experiment without lower conveyor speeds and low peak temperatures. Conveyor speed was kept constant during firing.

Experiment 3: At this point, we changed our paste supplier and Paste B was used. After cross experiments were done in Germany and Turkey, we planned experiment 3 and 4. Experiment 3 includes optimization of physical properties of the back Al paste.

Experiment 4: This experiment consists of re-optimization of firing furnace parameters for paste B that gave us the final optimized firing parameters.

Experiment 5: In this experiment volatile compounds are investigated with EDX analysis.

A) Experiment 1

In this experiment, all zones of the furnace were activated and temperatures were set as shown in Table 4.5. 3 sets of experiments were done. In the first set, the entrance speed was set to 25 mm/s, peak temperature was 870°C and hot zone speeds were compared (50-75-100 mm/s). In the second set, entrance speed was set to 100 mm/s, peak temperature was 870°C and hot zone speeds were compared (50-75-100 mm/s). In the third set, first set was repeated for 910°C peak temperature.

Table 4.5 Sample Firing Furnace parameters for experiment 1.

	Zone 1	Zone 2	Zone 3	Zone 4	Zone 5	Zone 6	Zone 7
Temp [°C]	100	300	650	775	870	775	600
Speed [mm/s]	25	25	25	100	100	100	25

Table 4.6 Firing parameters of Set 1, Set 2 and Set 3 of experiment 1.

Sample No	Entrance Speed [mm/s]	Hot Zone Speed [mm/s]	Peak Temperature [°C]
3	25	50	870
4	25	75	870
5	25	100	870
6	100	25	870
7	100	50	870
8	100	75	870
9	100	100	870
10	25	25	910
11	25	50	910
12	25	75	910
13	25	100	910

Results of experiment 1, set 1:

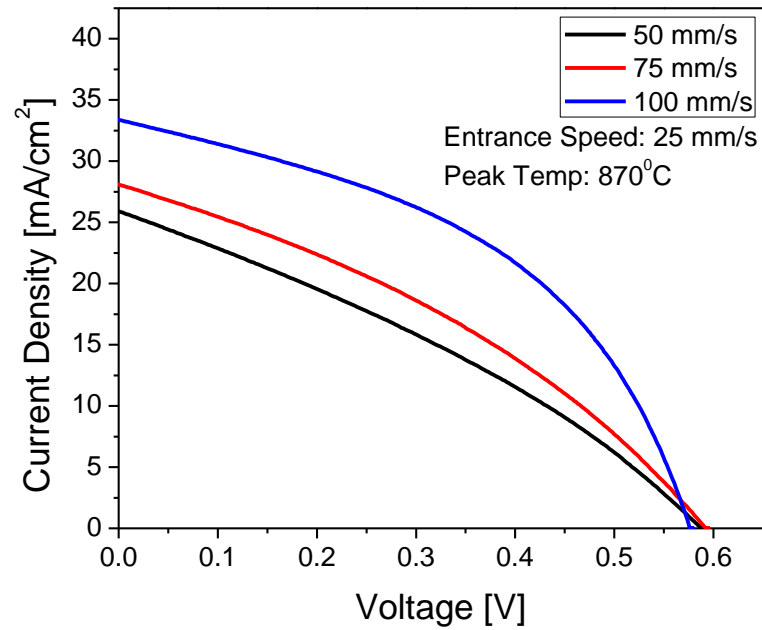


Figure 4.22 I-V curves of sample 3,4,5 with hot zone speed 50 mm/s, 75 mm/s and 100 mm/s while entrance speed is 25 mm/s. Peak temperature was 870°C (Cell area was 92.5 cm²).

Table 4.7 Results of experiment 1, set 1.

Sample No	Conv. Speed [mm/s]	Peak Temp. [°C]	V _{oc} [V]	I _{sc} [A]	FF [%]	Efficiency [%]	R _s [Ω]	R _{sh} [Ω]
3	50	870	0.5896	2.258	33.8	4.865	0.180	0.5
4	75	870	0.5927	2.433	37.2	5.799	0.145	0.6
5	100	870	0.5773	3.045	51.5	9.787	0.045	1.2

I-V curves measured with the solar simulator with standard A.M1.5 illumination and the cell performance parameters extracted from the I-V curves are shown in Figure 4.22 and Table 4.7, respectively. Results show that the cell performance improves with the conveyor speed. For low speed, the shunt resistance is low and the series resistance is high. It seems that low conveyor speed causes a shunt between the terminals of the cell. With increasing conveyor speed, the shunt resistance increases. We also observed improvement in the series resistance probably as a result of higher shunt resistance. In the second experiment set, we increased the zone speed to 100 mm/s.

Results of experiment 1, set 2:

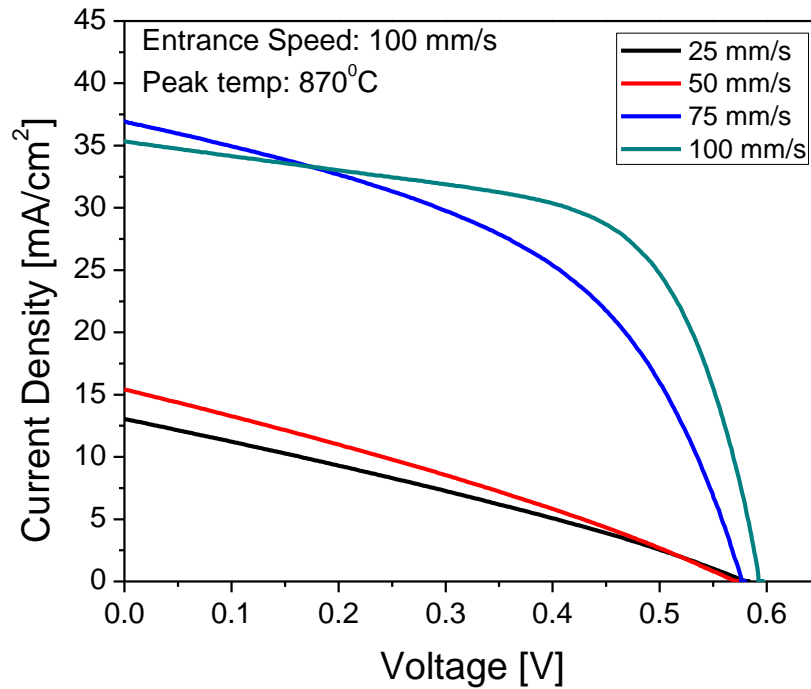


Figure 4.23 I-V curves of sample 6,7,8,9 with hot zone speed 25mm/s, 50 mm/s, 75 mm/s and 100 mm/s while entrance speed is 100 mm/s. Peak temperature is 870°C. Cell area is 92.5 cm².

Table 4.8 Results of experiment 1, set 2

Sample No	Conv. Speed [mm/s]	Peak Temp. [°C]	V _{oc} [V]	I _{sc} [A]	FF [%]	Efficiency [%]	R _s [Ω]	R _{sh} [Ω]
6	25	870	0.5823	1.160	30.0	2.190	0.433	0.8
7	50	870	0.5727	1.407	30.1	2.621	0.368	0.7
8	75	870	0.5787	3.143	54.6	10.736	0.039	1.1
9	100	870	0.5952	3.020	71.6	13.913	0.023	49.3

In Figure 4.23, we display the I-V curves of the solar cells for four different zone speeds. Again, the solar cell performance improved with the increasing zone speed. The cell parameters are displayed in Table 4.8. We see that we have reached an efficiency of 13.9% and fill factor value of 71% with the highest speed (100 mm/s). Lower zone speed is probably causing over-firing meaning that Ag paste diffuses into the substrate and shorts the p-n junction. At higher speed, the diffusion is not allowed so that the junction quality improves. In order to verify this prediction we conducted experiment set 3 with higher peak temperatures. Therefore, lower fill factors were attributed to the increased diffusion of Ag.

Results of experiment 1, set 3:

In this set, we expected to see lower fill factors because of the over firing. Sample 10-13 were tested at 910°C with variable hot zone speeds.

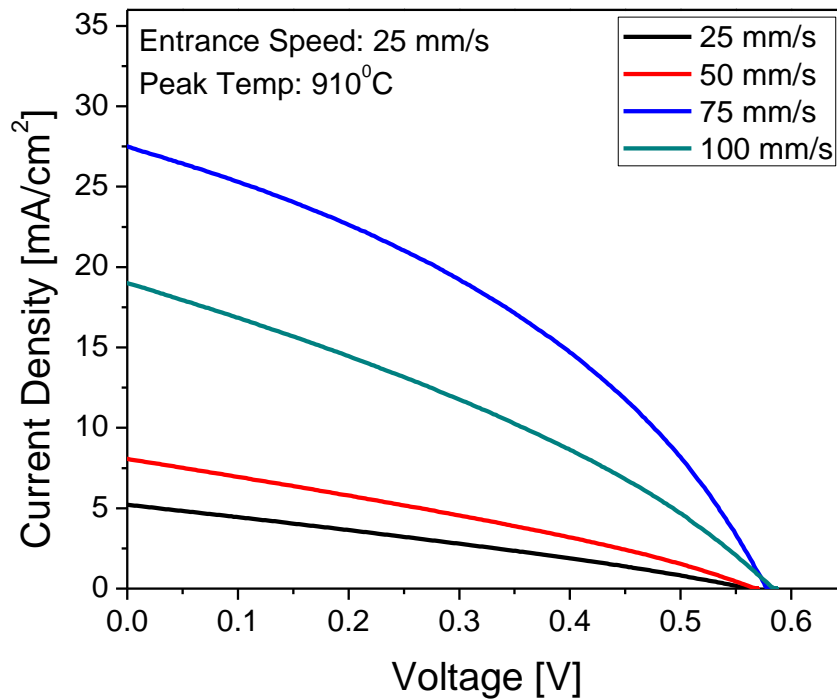


Figure 4.24 I-V curves of sample 10,11,12 and 13 with hot zone speed 25mm/s, 50 mm/s, 75 mm/s and 100 mm/s while entrance speed is 100 mm/s. Peak temperature was 910°C. Cell Area was 92.5 cm².

Table 4.9 Results of experiment 1, set 3

Sample No	Conv. Speed [mm/s]	Peak Temp. [°C]	V _{oc} [V]	I _{sc} [A]	FF [%]	Efficiency [%]	R _s [Ω]	R _{sh} [Ω]
10	25	910	0.5636	0.497	29.2	0.884	1.160	1.8
11	50	910	0.5692	0.727	31.3	1.400	0.634	1.3
12	75	910	0.5799	2.527	41.6	6.590	0.113	0.8
13	100	910	0.5861	1.749	34.7	3.845	0.236	0.7

As we anticipated, fill factors were low. To avoid this problem, the upper limit of firing process was established. Results of over firing were discovered with resistive 7 zone firing furnace. As a next step, in experiment 2, lower temperatures were investigated.

B) Experiment 2

In experiment 1, we identified the upper limits of firing process by adjusting peak temperatures and conveyor speeds. In experiment 2, we aimed to find differences in IV-curves at lower temperatures. In this experiment, we used paste A again. Since we studied the lower conveyor speeds in detail in previous section, these parameters were not studied in this experiment. Entrance and hot zone speeds were kept equal. In the first set, the peak temperature was 870⁰C and conveyor speeds were 70, 80, 90 mm/s. In set 2, conveyor speed was kept at 90 mm/s and the peak temperature was varied between 860-890°C. In the third set, the same experiment was performed with 70 mm/s conveyor speed.

Table 4.10 Firing parameters of the samples which are used in experiment 2

Sample no	Speed [mm/s]	Temp [°C]
2	70	870
3	80	870
4	90	870
5	90	860
6	90	880
7	70	860
8	70	850

Results of experiment 2, Set 1:

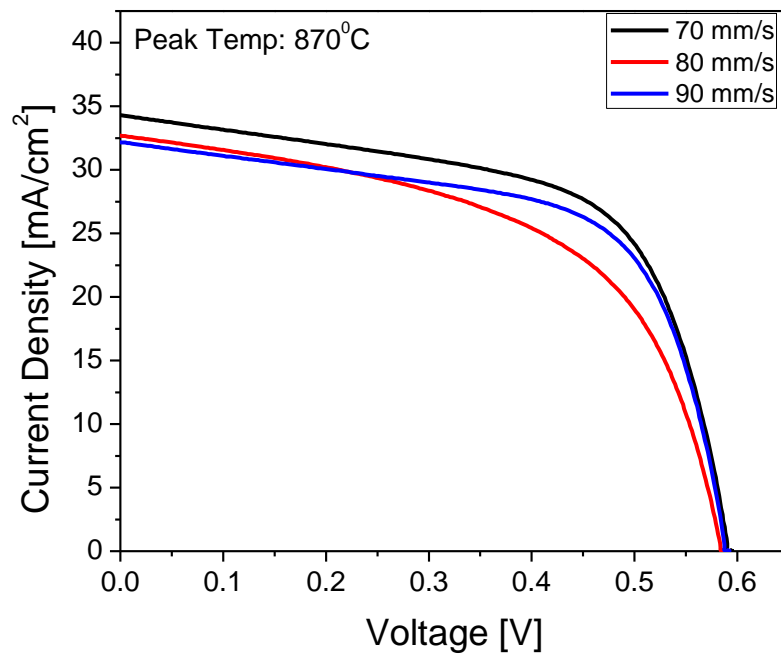


Figure 4.25 I-V curves of sample 2, 3, 4 with conveyor speed 70 mm/s, 80 mm/s and 90 mm/s, while peak temperature was 870°C. Cell area was 92.5 cm².

Table 4.11 Results of experiment 2, Set 1

Sample No	Conv. Speed [mm/s]	Peak Temp. [°C]	V _{oc} [V]	I _{sc} [A]	FF [%]	Efficiency [%]	R _s [Ω]	R _{sh} [Ω]
2	70	870	0.5937	3.033	72.2	14.055	0.020	13.2
3	80	870	0.5861	2.908	63.4	11.682	0.026	12.1
4	90	870	0.5918	2.660	73.3	12.473	0.022	13.2

Measured I-V curves and solar cell parameters extracted from these curves are shown in Figure 4.25 and Table 4.11, respectively. We see further improvement in the cell parameters compared to previous experiments. We have achieved an efficiency value of 13.9 % in this experiment set. However, the variation of the conveyor speed was not significant.

In the second set, conveyor speed was kept constant at 90 mm/s and peak temperature was changed between 860-890°C.

Results of experiment 2, Set 2:

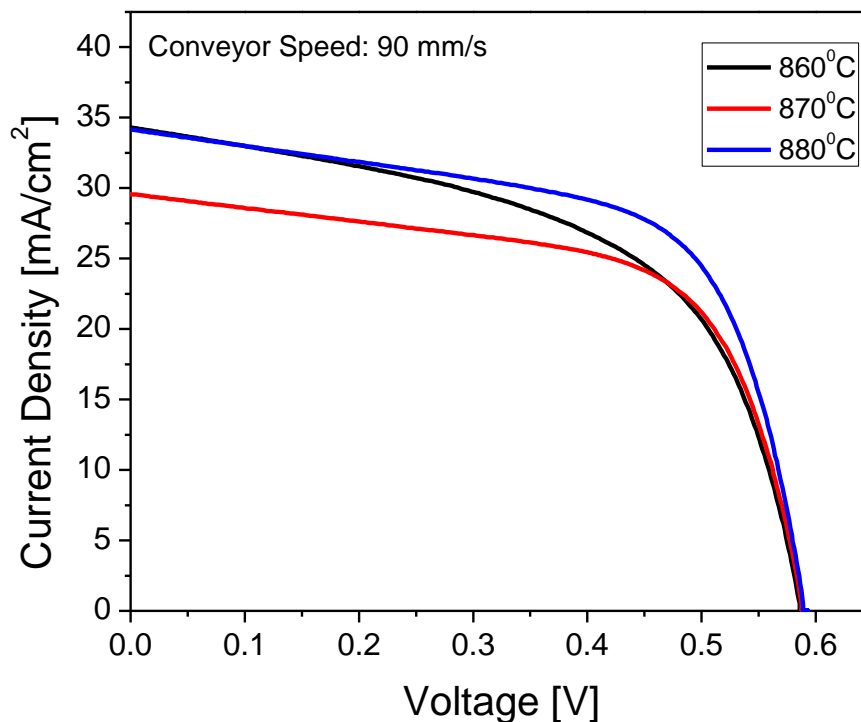


Figure 4.26 I-V curves of sample 5, 4, 6 respectively with peak temperatures 860°C, 870°C and 880°C, while conveyor speed was 90mm/s. Cell area was 92.5 cm².

Table 4. 12 Results of experiment 2, Set 2

Sample No	Conv. Speed [mm/s]	Peak Temp. [°C]	V _{oc} [V]	I _{sc} [A]	FF [%]	Efficiency [%]	R _s [Ω]	R _{sh} [Ω]
5	90	860	0.5883	3.035	64.3	12.411	0.024	3.8
4	90	870	0.5889	2.660	73.3	12.413	0.022	13.2
6	90	880	0.5883	3.021	73.3	14.083	0.019	8.9

Results of this set are shown in Figure 4.26 and Table 4.12. We see that we have further improved the cell performance with this set of process conditions. 890⁰C degree was found to be the best firing temperature. However, increasing temperature caused some other problems such as bumps on the back surface Al. This problem can be seen in Figure 4.27. To overcome this problem, we planned to reduce temperature and slowing down the conveyor speed. By this method, we could keep same the firing ratio while decreasing the temperature.



Figure 4.27 Bump problems on back Al paste.

Results of experiment 2, set 3:

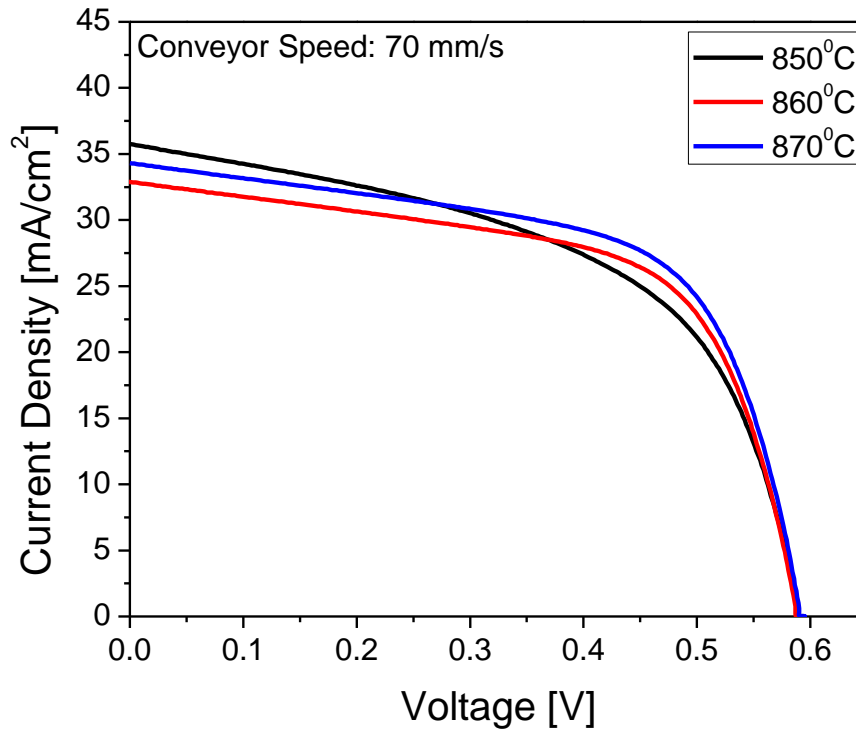


Figure 4.28 I-V curves of sample 8,7,2 respectively with peak temperatures 850°C, 860°C and 870°C, while conveyor speed was 70mm/s. Cell area was 92.5 cm².

Table 4. 13 Results of experiment 2, set 3

Sample No	Conv. Speed [mm/s]	Peak Temp. [°C]	V _{oc} [V]	I _{sc} [A]	FF [%]	Efficiency [%]	R _s [Ω]	R _{sh} [Ω]
8	70	850	0.5924	3.150	62.6	12.628	0.024	2.2
7	70	860	0.5881	2.922	72.1	13.394	0.021	9.9
2	70	870	0.5905	3.033	72.2	13.979	0.020	13.2

The results of this set are shown in Figure 4.28 and Table 4.13. We see the best cell performance was achieved at the highest temperature studied. However, the bump problem couldn't be solved. In order to address this problem, we changed the paste since each paste has a different "bump resistivity". In the following experiments, Paste B with a higher bump resistivity was used.

C) Experiment 3

Before starting optimization of firing with paste B, we visited Ferro GmbH's screen printing lab in Hanau, Germany. The experiments conducted in this lab are separately discussed in Section 4.6. Following the analysis of the experiments done in Hanau, we started the optimization of the new paste with the bump characterization of the Al paste. Purpose of this experiment was to find maximum firing temperature without any bump. In experiment 3, seven different peak temperatures and three different conveyor speeds were tested. Process conditions and results of bump and bow formation can be seen in Table 4.14.

Table 4.14 Experimental conditions giving bumps and bows on the back Al metal layer.

Peak Temp. [°C]	Belt speed [mm/s]	Bump	Bow [mm]
880	90		0.6
880	70		0.8
880	50	Yes	1
870	90		0.7
870	70		1.1
860	90		1
860	70		0.9
850	90		1
850	70		1.1
840	90		1
840	70		1
840	50	Yes	1
830	90		0.7
830	70		0.8
830	50		0.9
820	90		0.6
820	70		1.2

As seen in Table 4.14, bump formation was not observed with the new paste. Only very slow conveyor speeds (50 mm/s) caused bumps on the Al paste. This means, over firing limit of the Paste B is higher than Paste A. Experiments 1 and 2 were repeated with the new paste to see the positive effect of new paste on the cell performance.

D) Experiment 4

In this experiment, only three zones were activated to get simpler and sharper temperature profiles. The obtained temperature profile was close to the temperature profile of IR furnace used in Germany. In addition, according to the previous experiences, only the highest speed of the furnace was used: 90 mm/s. Three different firing temperatures were tested in this experiment; which are 850°C, 870°C and 880°C. Lower temperatures couldn't fire paste and some wet areas were remained on the Al paste. The cell parameters extracted from the I-V curves are shown in Table 4.15.

Table 4.15 Firing temperatures and corresponding cell parameters obtained from the I-V curves of the samples fabricated using paste B.

Sample No	Peak Temp [°C]	I _{sc} [A]	V _{oc} [V]	FF	Efficiency [%]
1	880	7.88	0.610	0.705	14.19
2	880	7.66	0.608	0.731	14.27
3	880	7.78	0.612	0.678	13.52
4	880	7.86	0.610	0.709	14.23
5	870	7.96	0.609	0.727	14.77
6	870	7.90	0.609	0.710	14.31
7	870	7.88	0.611	0.711	14.33
8	870	7.89	0.607	0.731	14.68
9	850	7.87	0.609	0.718	14.42
10	850	7.95	0.608	0.729	14.78
11	850	7.93	0.605	0.729	14.65
12	850	8.07	0.602	0.723	14.71

4 different sample sets were fabricated with the same process parameters and averages of I_{sc}, V_{oc} FF and efficiencies are plotted in Figure 4.29 and 4.30.

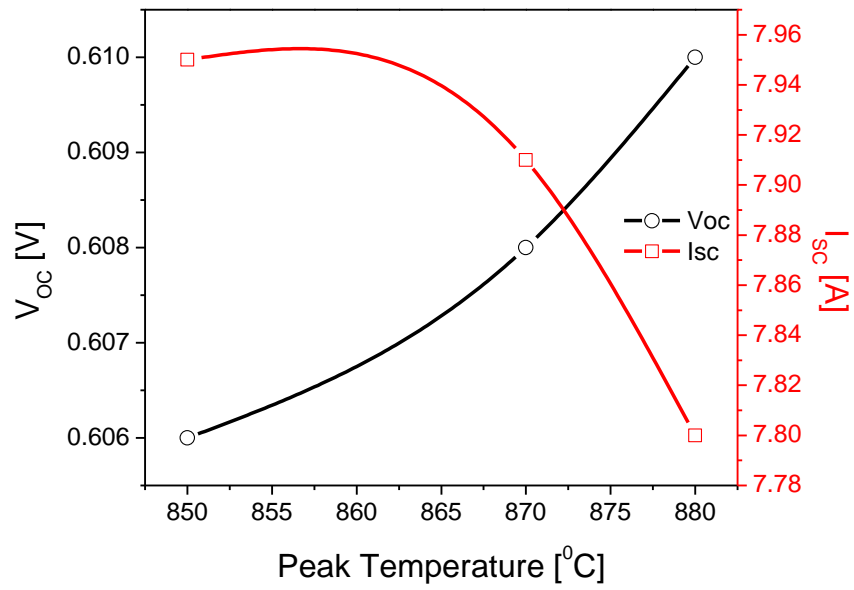


Figure 4.29 Peak temperature dependency of open circuit voltage and short circuit current.

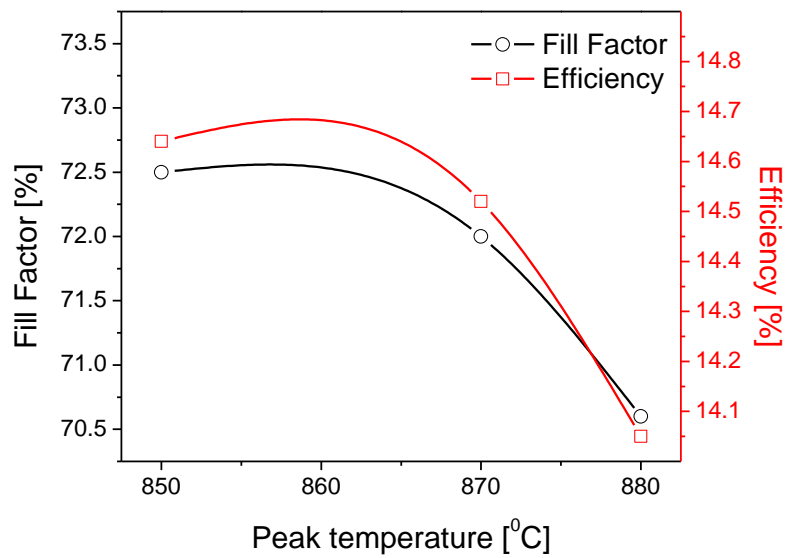


Figure 4.30 Peak temperature dependence of fill factor and efficiency.

It is seen that the short circuit current decreases while the open circuit voltage increases with the firing temperature. This means that the collection efficiency decreases while the overall quality of the diode improves with lower firing temperatures. This can be understood by looking at fill factor values. We see that the fill factor decrease with the firing temperature. It can be explained by the increase in the shunt resistance due to over diffusion of Ag paste. Decrease on the V_{oc} can also be explained by the decrease in the p-n junction quality and series resistance.

As a result, we conclude that the short circuit current is more dominant in determining the studied solar cells. Correlated with the short circuit current we see that fill factor and efficiency decreases with increasing firing temperatures. In this experiment set, we have achieved an efficiency value of %14.65 at a firing temperature of 850 °C. Lower firing temperatures left wet spots on Al layer, which is not preferred. In later experiments, 850°C firing temperature with 3 active zones and 90 mm/s conveyor speed was employed as the standard firing recipe.

E) Experiment 5

In this experiment, ingredients of Al and Ag pastes are investigated. Since chemical formulas of the pastes are commercial secrets, it is hard to find polymers which are used as binders. In this experiment we investigated the effect of firing on the pastes. We expected removal of some elements inside the pastes. Especially organic compounds are volatile at high temperatures. As seen in figure 4.31 K, Ti and Co completely vanished after firing in Al paste. K and Fe were also vanished in firing process in Ag paste. As expected Carbon concentration decreased with firing process.

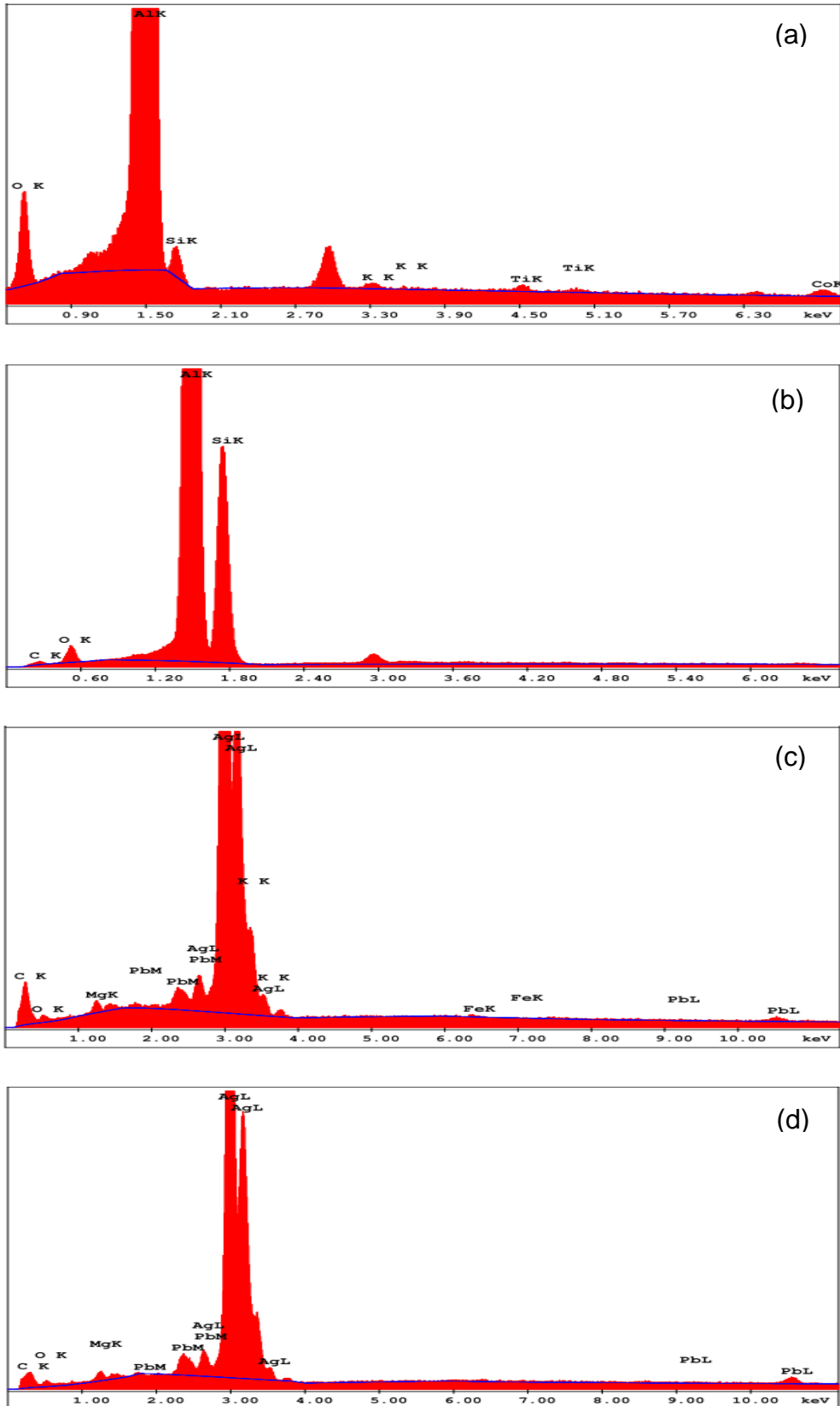


Figure 4.31 EDX results of pastes a) Al paste before firing b) Al paste after firing c) Ag paste before firing d) Ag paste after firing

4.5.2. Back Surface Field optimization

One of the main functions of firing is to create “Back Surface Field” (BSF) on the back side of the cell. However, it is also very important to reduce the carrier recombination at the back surface. In this study, three different firing temperatures and three different conveyor speeds were tested to characterize BSF created by the Al layer printed on to the back surface.

As a characterization method, two different tests were applied, namely Sheet Resistance and SIMS (Secondary Ion Mass Spectrometry) measurements. Sheet resistance provided electrical data, while SIMS results give information about the atomic concentrations.

For the sheet resistance measurements the Al film was removed from the back surface after diffusion and the sheet resistance of the doped surface was measured by a four point probe technique. As can be seen in Table 4.16 and Figure 4.31, the sheet resistance decreases with increasing firing temperature. As expected, more Al atoms diffuse into the substrate and results in a lower sheet resistance at higher firing temperatures and lower conveyor speed. This is well correlated with the SIMS results shown in Figures 4.32 and 4.33. SIMS data proves that the amount of Al is less for high conveyor speed and low firing temperatures. So, we can conclude at this point that the BSF is successfully created on the back surface of the cell by the Al diffusion process during high temperature firing.

Table 4.16 Applied recipes and obtained sheet resistances.

	Conveyor Speed [mm/s]	Firing Temp. [°C]	Sheet Resistance (Ω /Sq)
T1	90	900 °C	19.85
T2	50	900 °C	13.49
T3	20	900 °C	8.36
T4	90	830 °C	21.03
T5	50	830 °C	16.58
T6	20	830 °C	12.61
T7	90	750 °C	83
T8	50	750 °C	61
T9	20	750 °C	16.12

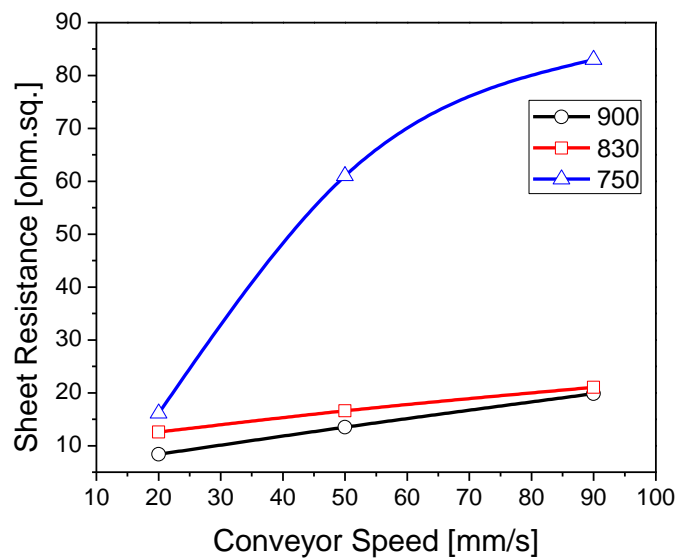


Figure 4.32 Firing dependence of back surface sheet resistance.

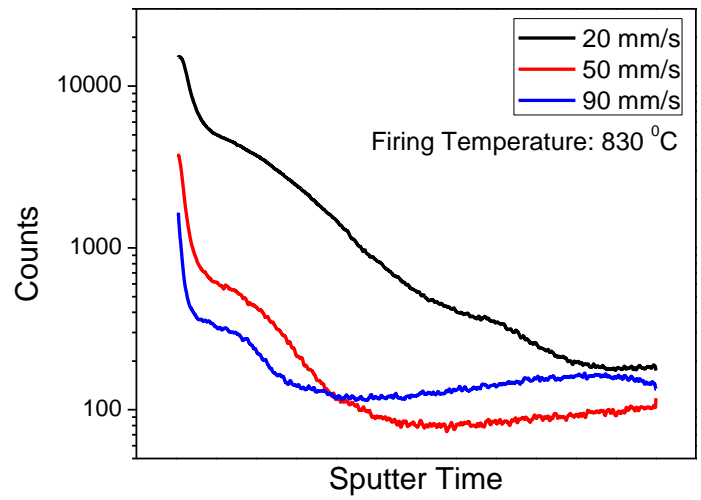


Figure 4.33 Conveyor speed dependence of back surface field depth.

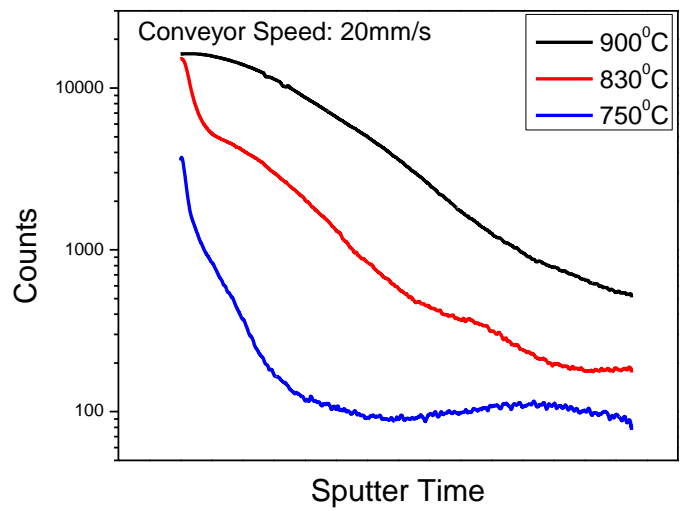


Figure 4.34 Firing temperature dependence of back surface field depth.

We see that the higher the temperature we use the better the BSF formation. However, it is not possible to make firing with 900⁰C and/or 20mm/s because of over-firing effects on front surface metallization.

4.6. Cross Experiments in Ferro GmbH

The purpose of the cross experiments was to perform the same processes with same materials in Ferro Facility in Germany and GÜNAM and compare the results. Ferro is a well-known company producing metallization pastes. The company has a well-equipped R&D laboratory in Hanau, Germany. We visited Ferro facility and did the same experiments there together. This visit contributed also to our overall process experience.

The experimental study in Hanau included printing, drying, firing, cell testing, finger geometry characterization and laser edge isolation. Laser edge isolation is out of the scope of this thesis; but, it was a supportive study to compare our edge isolation process with the same process done in University of Aachen. After one week study in Ferro Labs, same optimization processes were performed in GÜNAM Laboratories.

There were two main processes we focused on, namely screen printing and firing. In order to get detailed results and compare with our lab, we prepared 3 different sample sets. All production processes such as etchings, doping, anti-reflection coating were done in GÜNAM Labs before cross experiments. Corresponding labs to different sets of samples and achieved efficiencies are given in Tables 4.17 and 4.18.

Table 4. 17 Sets of cross experiment with Ferro GmbH and GÜNAM

	Printing Lab	Firing Lab
Set 1	Hanau	Hanau
Set 2	Hanau	GÜNAM
Set 3	GÜNAM	GÜNAM

Table 4.18 Average efficiency results of cross experiments

	Average Efficiencies
Set 1	15.12%
Set 2	14.83%
Set 3	15.26%

After these cross experiments, we exceeded the 15% photovoltaic conversion efficiency. We also proved that our printing quality after the optimization study carried out during this study is as good as Ferro Lab's. It was also shown that there is no important difference between IR furnace of Ferro Lab and our resistive firing furnace performance.

Finger homogeneity was another output of this cross experiment. A laser surface scanner in Ferro Labs was used to scan samples from set 1 and representative scan is provided in Figure 4.34

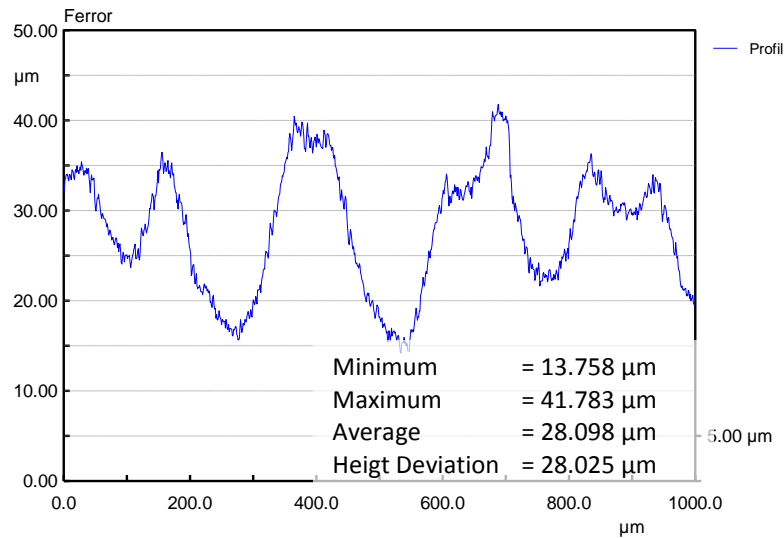


Figure 4.35 Finger homogeneity characterization of a sample from Set 1.

Finger scanning showed that height deviation on the samples, which are optimized in Ferro has 28 microns of deviation on height. As given in section 4.3.5, we achieved 13-14 microns of deviation, which is even better than Ferro's values.

4.7. Fabrication of a High Efficiency Solar Cell at GÜNAM Laboratories

This optimization study included metallization quality and effects of firing on the paste diffusion. As a result of this study, the efficiency of a 6 inch c-Si solar cell was improved from 10.09 % to 15.25 %. Parallel to these experiments, other production steps (surface texturing, doping process, anti-

reflection (Si_3N_4) coating and edge isolation processes) were also optimized by GÜNAM researchers.

As a result of surface texturing step, homogenous and regularly distributed pyramids were obtained with minimum reflection. Optimization of doping process yielded homogeneously doped wafer surfaces. The anti-reflection coating was also studied to obtain best condition for the refractive index, absorption coefficient and the homogeneity.

When all optimization results are combined, highly efficient mc-Si solar cell was obtained with an efficiency of 17 %. Images of this cell are provided in Figure 4.35. Electrical parameters and I-V curve of the cell is given in Figure 4.36.

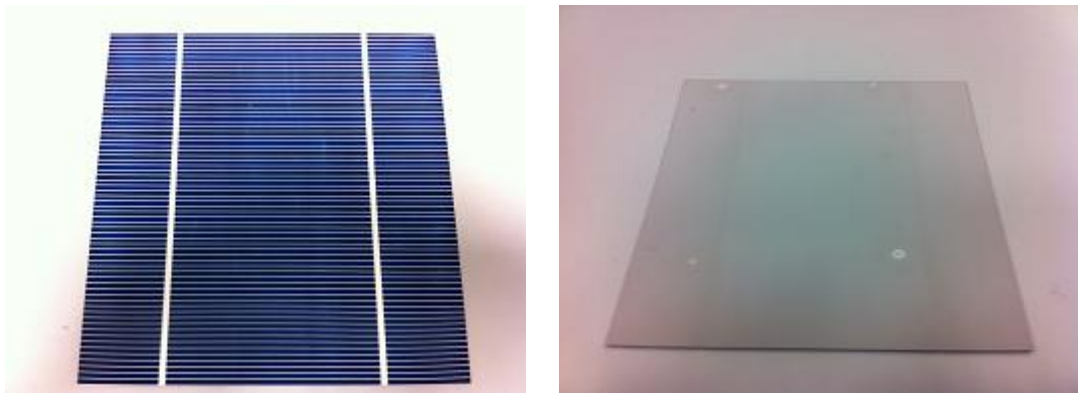


Figure 4.36 Front and back view of 17 % efficient solar cell fabricated in GÜNAM Laboratories.

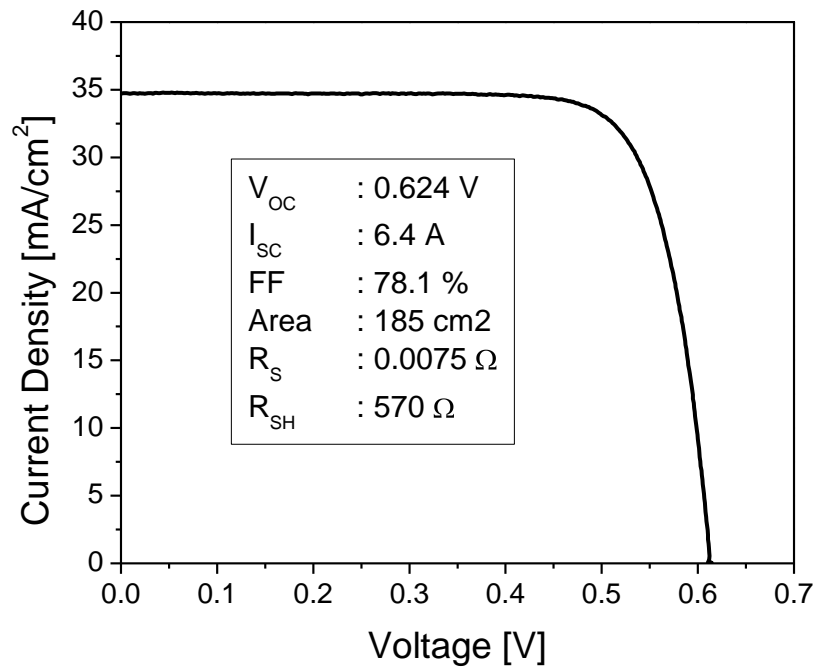


Figure 4.37 I-V Curve of highly efficient c-Si solar cell.

Parallel to this study, other processes (etching, texturing, doping, Si_3N_4 coating, edge isolation) were optimized. Combination all of these optimization studies yielded the high efficiency c-Si solar cell with a photovoltaic conversion efficiency of 17%. The milestones during this collective optimization study are shown in figure 5.1. We see that the progress in the metallization process had important impacts on the efficiency of fabricated solar cells.

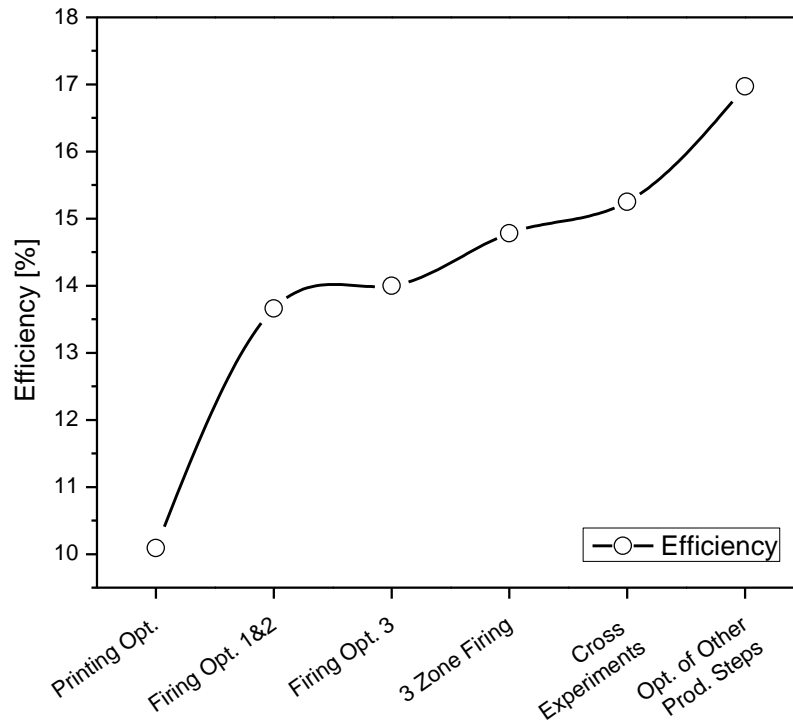


Figure 4. 38 Progress in the efficiency values of c-Si solar cells fabricated at GÜNAM Laboratories

CHAPTER 5

CONCLUSION

The aim of this study was to understand the effect of metallization on the cell performance and optimization of this process towards the fabrication of highly efficiency solar cells. For the metallization process, we have used screen printing technique, which is the standard technique in solar cell production lines. 6 inch standard mono crystalline silicon wafers were used during this study. All process steps were carried out at GÜNAM Facilities. Since metallization is the last production step, sample preparation included saw damage etching, surface texturing, doping and SiNx coating were completed prior to metallization experiments. The edge isolation step was replaced with an edge removing step to ensure the reduction of edge shunts.

In the first part of this work, drying and firing dependence of the contact resistance of metallization pastes were studied. It was observed that contact resistance is not sensitive to the drying or firing parameters.

In the second part, effects of the screen printing parameters to the front surface metallization were studied. The purpose of this study was to obtain the best aspect ratio for fingers. It was observed that, increasing squeegee speed decreased the finger width while increasing the finger height. Consequently, the aspect ratio increased with higher squeegee speeds. However, 200mm/s squeegee speed caused some disconnection on fingers. Therefore, 100 mm/s squeegee speed was chosen as the optimum squeegee speed.

Another printing parameter, squeegee pressure was also effective on finger aspect ratio. Squeegee pressure was studied between 0 to 3.5 bars. This study showed that increasing pressure decreases the aspect ratio. However, lower pressures caused some discontinuities in the fingers. At the end of this optimization study, 1.3 bars squeegee pressure was chosen as the processing parameter.

As a result of optimization of first two parameters, 23.7% aspect ratio was achieved. Snap off, which is the gap between cell and printing mask was found to have a minor effect on the aspect ratio. It was noticed that, increasing snap off increases the aspect ratio slightly. However, we determined that larger snap off prevents metal paste to stick on wafer, and for this reason, 0.6 mm snap off gave the best printing quality.

Screen printed fingers were not as homogeneous as evaporation. There was always a thickness fluctuation on printed thick films. This fluctuation was characterized with surface profilometer and a fluctuation of 14 μm was observed with optimized parameters. It was found that the fluctuation is acceptable and similar to that seen in the fingers of commercial solar cells.

Optimization of back surface metallization was aimed to obtain the best homogeneity in thick Al film over the back surface. Since printed area was too large, non-homogeneity of printing caused stress problem. This problem was solved by decreasing snap off to zero and squeegee pressure to 0.6 bars.

Dependence of the amount of metal paste used on squeegee speed, squeegee pressure and snap off were also investigated. Although metal amount used on the back side was not important for cell performance, this can have a significant effect on the production cost. While increasing snap off and squeegee speed increased the amount of paste on wafer, increasing squeegee pressure had an opposite effect on the amount of paste as expected. When optimized we have reached mass values that are within the acceptable industrial range.

During this study, we found that the most sensitive factor on the efficiency was the firing process. We used two different pastes and optimized firing parameters twice. After having used different metal pastes, we found that, firing parameters are specific to the type of the paste and firing furnace. Results showed that 3 zone firing with 830°C peak temperature was optimum for our furnace system. Higher temperatures caused over diffusion of Ag and shunt resistances decreased rapidly. Another hazard of the over firing is bump creation on Al paste. Since bump resistivity of Paste A was not enough, we started use Paste B to overcome bump problem.

Lower temperatures resulted in low efficiencies because of two possible reasons. First, lower temperatures were not enough to evaporate solvents and resins in the metals paste. Therefore, Al paste's resistivity couldn't decrease enough and created series resistance. Second possible problem with low firing temperatures was low back surface field creation. We observed that Al concentration on the back surface is directly related with the firing temperature.

Conveyor speed affected the results in the same way as the firing temperature. Lower conveyor speeds caused over firing. For this reason, we determined the maximum possible conveyor speed (100mm/s) is the best speed. 4 different experiments were performed with different sample sets and it was shown that 100 mm/s conveyor speed with 830°C peak firing temperature yielded best metallization process. It is important to note that the similar optimization experiment should be repeated if another paste from a different manufacturer is going to be used.

For the further studies, new screen printing masks should be designed and thinner fingers about 80-90µm should be achieved. To be able produce high efficiency solar cell designs, such as back contact or buried contact solar cells, alternative metallization techniques should be studied and optimized. Although it is not as practical as screen printing, electroless plating method can be superior for these innovative designs.

REFERENCES

- [1] "New National Energy Strategy," Ministry of Economy Trade and Industry of Japan, 2006.
- [2] "PV Market Research," IMS Research, [Online]. Available: http://imsresearch.com/tiny_mce/plugins/imagemanager/files/PV_Blogs/PV_Module_Costs_and_Prices_Blog/PV_Module_Costs_and_Prices_Blog.jpg. [Accessed 15 05 2012].
- [3] P. E. Sach, "The tech Journal Technological News Portal," Green Tech, 22 11 2011. [Online]. Available: <http://thetechjournal.com/green-tech/a-recent-discovery-could-double-solar-panels-efficiency.xhtml>. [Accessed 29 07 2012].
- [4] "Promotion of the Use of Energy from Renewable Sources and Amending and Subsequently," European Union, The European Union - Parliament and the Council of the European, 2009.
- [5] E. P. I. A. EPIA, "Global Market Outlook," 2012.
- [6] M. A. Green, "Silicon Photovoltaic Modules: A Brief History of the First 50 Years," *Progress in Photovoltaics*, vol. 13, pp. 447-455, 2005.
- [7] M. Bellis, "About Inventors," New York Times, [Online]. Available: <http://inventors.about.com/od/timelines/a/Photovoltaics.htm>. [Accessed 29 07 2012].
- [8] A. Goetzberger, J. Luther and G. Willeke, "Solar cells: past, present, future," *Solar Energy Materials & Solar Cells*, vol. 74, pp. 1-11, 2002.
- [9] F. Cavallaro, "A comparative assessment of thin-film photovoltaic

- production processes using the ELECTRE III method," *Energy Policy*, vol. 38, pp. 463-474, 2010.
- [10] B. Sopori, "Thin-film Silicon Solar Cells," in *Handbook of Photovoltaic Science and Engineering*, John Wiley & Sons, Ltd, 2003, pp. 307-357.
- [11] W. N. Shafarman and L. Stolt, "Cu(InGa)Se₂ Solar Cells," in *Handbook of Photovoltaic Science and Engineering*, John Wiley & Sons, Ltd, 2003, pp. 367-616.
- [12] L. B. e. al., *Solar Energy Materials & Solar Cells*, vol. 90, pp. 549-537, 1982.
- [13] R. Akhter and . A. Hoque, "Analysis of a PWM Boost Inverter for Solar Home Application," in *World Academy Of Science, Engineering And Technology*, 2006.
- [14] P. Würfel, *Physics of Solar Cells*, Wiley VCH Verlag GmbH & Co, 2005.
- [15] A. Goetzberger, J. Knobloch and B. Voss, *Crystalline Silicon Solar Cells*, Wiley & Sons Ltd., 1998.
- [16] A. Luque and S. Hegedus, *Handbook of Photovoltaic Science and Engineering*, John Wiley & Sons Ltd, 2003.
- [17] M. Pagliaro, G. Palmisano and R. Ciriminna, *Felxible Solar Cells*, Wiley-VCH, 2008.
- [18] J. Hvlton, "Wet chemical etching for crystalline silicon solar cells".
- [19] F. Es, *Fabrication and Characterization of Single Crystalline Silicon Solar Cells*, Middle East Technical University, 2010.
- [20] Solland Solar, [Online]. Available: www.sollandsolar.com. [Accessed 15. 05. 2012].

- [21] A. R. Burgers, *New Metallization Patterns and Analysis of Light Trapping for Silicon Solar Cells*, Utrecht University, Netherland, 2005.
- [22] M. A. Green, *Solar Cells: Operating Principles, Technology, and System Applications*, Prentice Hall, 1981.
- [23] D. Erath, A. Filipovic, M. Retzlaff, A. K. Goetz, F. Clement, D. Biro and R. Preu, "Advanced screen printing technique for high definition front side metallization of crystalline silicon solar cells," *Solar Energy Materials & Solar Cells*, vol. 94, pp. 57-61, 2010.
- [24] G. Schubert, F. Huster and P. Fath, "Physical understanding of printed thick-film front contacts of crystalline Si solar cells—Review of existing models and recent developments," *Solar Energy Materials & Solar Cells*, vol. 90, p. 3399–3406, 2006.
- [25] T. K. e. al., "The effect of firing temperature profiles for the high efficiency of crystalline Si solar cells," *Solar Energy materials and Solar Cells*, vol. 94, p. 823–829, 2010.
- [26] S. P. e. al., "Effects of controllable process factors on Al rear surface bumps in Si solar cells," *Current Applied Physics*, pp. 1-6, 2011.
- [27] «SSF,» SSF solar screen factory GmbH, [Çevrimiçi]. Available: <http://www.ssf.ag>. [%1 tarihinde erişilmiştir02 08 2012].
- [28] "PVCROM," Photovoltaic Education Network, [Online]. Available: <http://pvcrom.pveducation.org/RU/MANUFACT/SCRNPRT.HTM>. [Accessed 02 08 2012].
- [29] H. m. Tech., "Product Spotlight SOL9235H Series," [Online]. Available: http://pvsilverpaste.com/media/webmedia_local/media/pdf/Product_Spotlight_SOL9235H~2.pdf. [Accessed 02 08 2012].
- [30] N. D. Sankır, Metal-Semiconductor Contact Resistance and

Measurement Techniques, METU, 2002.

- [31] L. Shi, Contact Resistance Study on Polycrystalline Silicon Thin-Film Solar Cells on Glass, Sydney: School of Photovoltaic and Renewable Energy Engineering, 2008.
- [32] E. F. Schubert and J. M. Shah, "Specific Contact Resistance," [Online]. Available: <http://www.ecse.rpi.edu/~schubert/Course-Teaching-modules/A007-Specific-contact-resistance.pdf>. [Accessed 02 08 2012].
- [33] D. Erath, «Printing Techniques in the c-Si PV Industry- A brief Technological Overview,» 2009.
- [34] Big Sun Energy technology Inc., [Çevrimiçi]. Available: <http://www.bigsun-energy.com/en/>. [%1 tarihinde erişilmiştir02 08 2012].
- [35] B. R. Olaisen, A. Holt, E. S. Marstein, E. Saunar, A. Shaikh, J. Salami, H. Miranda ve S. S. Kim, «Hot Melt Screen Printing of Front Contacts on Crystalline Silicon Solar Cells».